A reduced-model (nSOLT) simulation of neutral recycling effects on plasma turbulence in the divertor region of MAST-U

D.A. Russell,[1] J.R. Myra[1] and F. Militello[2]

[1]*Lodestar Research Corporation, Boulder, Colorado 80301, USA*
[2]*CCFE, Culham Science Centre, Abingdon, Oxon OX14 3DB, United Kingdom*

October 2022
(revised February 2023)

accepted for publication in
Physics of Plasmas

DOE-ER/54392-100; SC0019270-4 LRC-22-192

LODESTAR RESEARCH CORPORATION
5055 Chaparral Court, Ste 102
Boulder, Colorado 80301

A reduced-model (nSOLT) simulation of neutral recycling effects on plasma turbulence in the divertor region of MAST-U

D.A. Russell and J.R. Myra
Lodestar Research Corporation, Boulder, CO 80301, USA

F. Militello
CCFE, Culham Science Centre, Abingdon, Oxon OX14 3DB, United Kingdom

Abstract

The 2D scrape-off-layer turbulence code (nSOLT), which includes 1D kinetic neutral-plasma interactions, is applied to study effects of neutral recycling on plasma turbulence for parameters illustrative of the MAST-U divertor region. Neutral recycling is modeled by injecting a fraction of the parallel plasma flux to the divertor back into the simulation domain as a source of Franck-Condon-distributed neutrals. Stationary sources, concentrated at the magnetic separatrix, model plasma streaming into the divertor region from the upstream scrape-off-layer (SOL) and sustain plasma turbulence absent neutral recycling. Starting from one such no-neutrals equilibrium, we initiate recycling in a numerical experiment designed to diagnose and identify the effects of various neutral-plasma interactions on the divertor plasma, divertor turbulence and plasma exhaust. The onset of recycling triggers an initial burst of enhanced cross-field plasma transport that is quelled by ionization cooling and charge-exchange (CX) friction, with growing neutral pressure, leading to a quiescent, turbulence-free state. Diagnosis of this transient burst reveals that 1) the sudden increase in plasma density due to ionization dominates the onset of the burst, 2) electron cooling due to ionization increases collisionality and disconnects blob filaments from the sheath, 3) CX friction drives *tripole* polarization of a blob that can dominate the curvature-driven dipole polarization, leading to the stagnation of blob propagation and reduced radial turbulent transport. It is shown that CX friction is negligible compared to sheath physics in determining equilibrium mean flow shearing rates, for parameters considered herein (specifically a short connection length to the divertor target), while it can significantly reduce interchange-instability growth rates.

I. Introduction

Neutral molecules and atoms are continuously emitted from the plasma-facing material surfaces in a tokamak and travel into regions of higher plasma density and temperature where they are dissociated and then ionized. Thus, the plasma is fueled by recycling. The neutral atoms (or “neutrals,” for short) are ionized by collisions with plasma electrons, and the electrons are cooled in the process. The neutrals also trade electrons with plasma ions through charge-exchange (CX) collisions which, in most cases of interest for tokamak experiments, tend to heat the neutrals and cool the ions. With increasing neutral density, charge-exchange and ionization (IZ) can change plasma profiles and fluctuation dynamics significantly.

Neutral-plasma interactions in a tokamak have the potential to alter characteristics of the plasma turbulence that impact the confinement properties of the device. Neutrals tend to degrade confinement in experiments. For example, the power threshold for the transition to the high-confinement mode has been observed to increase with neutral density on NSTX.[1] In some simulations, radial turbulent transport has been observed to rise, degrading confinement, due to the reduction in zonal flow (ZF) transport barriers caused by charge-exchange friction. [2, 3]

The impact of neutrals on plasma transport is potentially greatest in the neighborhood of the tokamak divertor where the highest neutral densities are found. There, for example, the neutrals can detach the upstream scrape-off layer (SOL) plasma from the divertor and so reduce, and spread-out, the plasma particle and heat fluxes at the divertor, importantly prolonging its lifetime.[4] (While heating by the plasma *energy* flux is moderated by increased radiation, the recombination load on the divertor from the plasma *particle* flux is significantly reduced only by detachment.) Recent validation studies, comparing turbulence simulations to a tokamak experiment, underscored the need to include neutral dynamics in the model equations, particularly in the neighborhood of the divertor.[5]

In previous studies, we benchmarked nSOLT [6] and studied the effects of neutral fueling on midplane profiles.[7] In the present paper, we model the environment of the MAST-U divertor and study the disconnection of blob-filaments from the divertor with increasing neutral density. We determine the nature of blob propagation following disconnection, how the plasma exhaust power is affected by disconnection, in peak power flux and width, and we determine the neutral interactions that are important for initiating disconnection and moderating instability and zonal flows in the disconnected state. For a review of the basic physics of blobs, the reader is referred to references [8] and [9].

Among the constantly evolving collection of numerical simulation codes used to describe neutral-plasma interactions in the tokamak, the nSOLT model is arguably the most reduced of the fluid-plasma, kinetic-neutrals *turbulence* simulation codes. More complete, but expensive-to-run, descriptions include the gyrokinetic PIC codes, exemplified by XGC1,[10] which model fluctuations down to the scale of the ion gyro-radius. Plasma fluid simulation codes are less expensive than PIC codes to run since they are limited to resolve turbulent fluctuations in the collisional plasma regime. The BOUT [11] and STORM [12] codes for example, and the many other fluid codes are based on the Braginskii fluid model equations,[13] as is nSOLT. (While the kinetic neutral model in nSOLT is one-dimensional (x,v_x), some neutral-plasma interaction codes use a similar kinetic description but hold the plasma profiles fixed and evolve the neutral distribution functions in greater than one velocity dimension.[14])

Among the fluid turbulence codes, the plasma evolution may be coupled either to a *fluid* description of the neutrals, exemplified by the BOUT++ framework with *trans-neut* module,[15, 16] the models of Bisai et al.,[17] and of Leddy et al.[18], and by the nHESSEL code of Thrysøe et al.,[19] or to a kinetic description of the neutrals, as in the GBS code of Wersal and Ricci,[20] and in nSOLT. The nSOLT code is similar to GBS, but where GBS models the entire tokamak in three dimensions, nSOLT applies a unique parallel transport model on the open field lines to reduce the simulation domain to the plane perpendicular to the magnetic field. In previous studies, that plane has been in the outboard midplane region of the tokamak, including the edge and SOL. In the present study, the simulation plane is in the X-point region near the divertor entrance. See Fig. 1. The introductions of references [6] and [7] offer more complete overviews of the simulation landscape.

The present work is concerned with effects of neutral interactions on plasma turbulence in the divertor region of the tokamak. Conditions in this region are known to support instabilities capable of driving turbulence, including the wall-induced electron temperature-gradient-driven instability,[21] beam-type instabilities of the plasma sheath,[22] the current convective instability,[23] instabilities driven by geodesic curvature[24] and by normal curvature such as the well-known interchange instability that drives the turbulence in our simulation.

In keeping with our mission of reduced modeling, our model divertor geometry is simpler than that found in other turbulence simulation codes that have machine-realistic divertor and magnetic field geometries. For example, the STORM module added to the BOUT++ framework [12] has been used recently to conduct fluid-plasma turbulence simulations of the divertor region in MAST[25] and to study detachment-induced changes in the dynamics of seeded filaments.[26] The GBS code was recently modified to include a divertor region by introducing X-point magnetic field geometry[27] and has been applied to study blob velocity scaling in a diverted tokamak.[28]

The nSOLT model offers a reduced version of large-scale simulations such as GBS and BOUT++/STORM. While these whole-machine codes include realistic divertor regions, their ability to resolve details of the turbulence in those relatively small sub-volumes of the simulation domain is constrained by computational resources. The reduced model simulation we describe herein focuses on a small neighborhood of the divertor region, enabling resolution of details essential for understanding the nature of neutral effects on plasma turbulence in that region.

The rest of the paper is organized as follows. Section II presents the nSOLT model equations, in brief, with details given in Ref. [7], and locates the simulation domain with respect to the divertor region in MAST-U. Section III presents results and analysis of a single nSOLT simulation: the turbulent response to a growing population of neutrals driven by plasma recycling at the divertor. Section IV presents parallel heat and particle flux diagnostics. Section V offers concluding remarks. Appendix A presents the derivation of a local, linear dispersion relation used in the analysis of results in Sec. III.

II. Model equations

a. Overview

The nSOLT model [7] describes the fluid plasma coupled to kinetic neutrals; it consists of four fluid equations of evolution for the plasma density (n_e), the electron and ion pressures (P_e and P_i) and the ion fluid vorticity ($-\rho$) that are coupled to the evolution of the neutral atoms by a kinetic equation. The domain of the simulation (x, y) is a plane perpendicular to the magnetic field, with the “bi-normal” variable (y) perpendicular to the B-field and to the magnetic flux gradient (“radial”) dimension (x). The kinetic equation evolves the y-averaged neutral distribution function, $G(x,v_x,t)$, in the radial dimension. Only the y-averages of plasma fields appear in the evolution of G, and the plasma sees neutrals that are homogeneously distributed in y. This aspect of the model significantly reduces the computation burden. Although the fundamental neutral-plasma interactions in the model remain valid in the short mean free path limit, this description is most appropriate for the neutrals in the long mean-free-path regime because in that case the neutrals average over plasma conditions in the y direction.

The nSOLT code was used in Ref. [7] to study turbulence in the outboard midplane (OM) region of the MAST-U tokamak. In the present study, the model is configured to describe the divertor region at MAST-U and does not include closed B-field lines nor (for simplicity) does it include an electron drift wave model as it did in Ref. [7]. See Fig. 1. In addition, the present implementation includes radiative (rr) and three-body (3r) recombination physics. The new recombination terms are proportional to the rate coefficients, h_{rr} and h_{3r}, appearing in the equations. Expressions for these coefficients are given in Eqs. (4e) and (4f) below.

The equations are in dimensionless (Bohm) units: time is measured in units of the ion gyro period (Ω_{ci}^{-1}), energies ($e\phi$, T_e, T_i) in units of a reference temperature (T_r), velocities in units of the corresponding cold ion acoustic speed ($c_{sr} = [T_r/m_i]^{1/2}$), length in units of the reference ion gyro-radius (ρ_{sr}) based on the sound speed ($\rho_{sr} = c_{sr}$ (Ω_{ci}^{-1}), and density is in units of a reference density (n_r). We adopt fundamental parameters illustrative of a deuterium plasma in the divertor region at MAST-U, at the reference location indicated by the red dot in Fig. 1: B = 7200 Gauss ($\Omega_{ci} = 3.45 \times 10^7$ rad/sec), curvature radius R_m = 90 cm, and connection length to the nearby target $L_{||}$ = 131 cm as determined by field-line tracing from a magnetic equilibrium reconstruction. These parameters result in the reference values c_{sr} = 69 km/sec and ρ_{sr} = 2 mm for the simulation, where the arbitrary reference temperature was chosen to be T_r = 100 eV.

This study does not analyze particular shots from MAST-U. Rather it began before MAST-U operations and was, and is, intended to address general fundamental physics phenomena relevant to divertors. The magnetic geometry is a generic MAST-U reference Fiesta equilibrium case for a conventional divertor. Nor did we use reference plasma profiles in the simulations. The simulation profiles adjust self-consistently in the course of evolution, balancing sources against losses. The typical width of the exhaust channel in the divertor region at MAST-U determined the shape and location of the source profiles shown in Fig. 2.

Convection is by the E×B velocity, $\mathbf{v}_E = \mathbf{b} \times \nabla\phi$, in a constant, uniform magnetic field $\mathbf{B} = \mathbf{b}B$ directed out of the (x,y) plane. The model considers only electrostatic fluctuations, where ϕ is the electrostatic potential. We summarize the model equations of evolution here and refer the reader to Ref. [7] for a more thorough description.

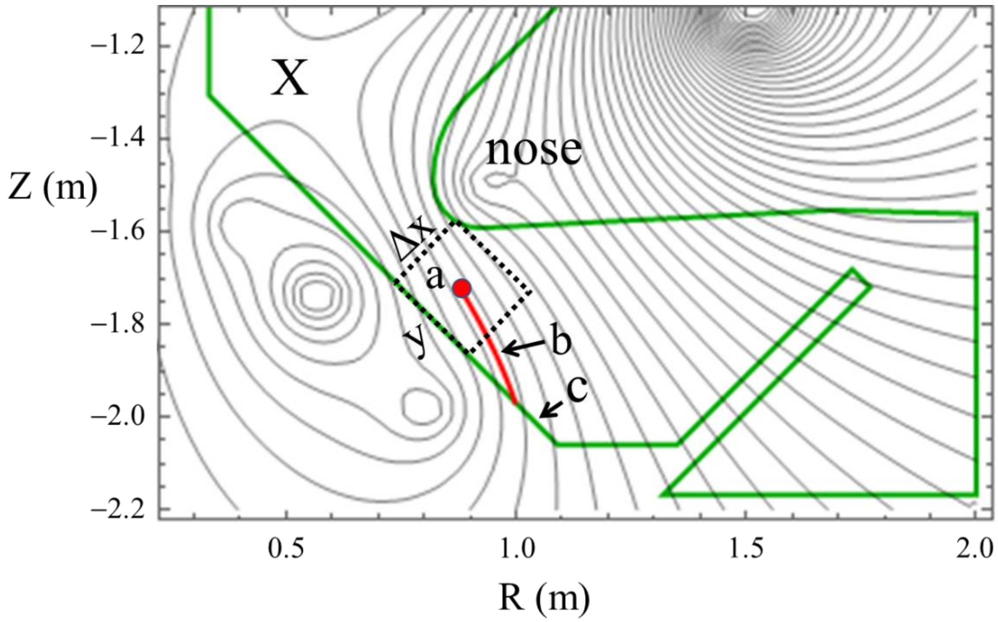

Fig. 1. The simulation plane (dashed, projected onto the RZ plane) is located within the divertor region of MAST-U, below the lower X-point and near the "nose" of the material wall (green). Contours of constant magnetic flux are shown in the background. The simulation magnetic field strength is measured at the reference point (a), and the connection path (b) follows a magnetic field line out of the plane of the simulation to the divertor face (c).

b. Plasma density

The equation of evolution of the plasma density ($n = n_e = n_i$) is

$$\partial_t n + \nabla_\perp \cdot (\mathbf{v}_E n) = S_n + \nabla_\perp \cdot (D_n \nabla_\perp n) - \nabla_{||}\Gamma_{||e} + h_{iz} n_0 n - h_{rr} n^2 - h_{3r} n^3 \qquad (1a)$$

where $\nabla_\perp = e_x \partial_x + e_y \partial_y$. S_n is a stationary source of plasma; the diffusion coefficient D_n was taken to be a constant equal to 0.3 m^2/sec, and the parallel gradient of the particle flux is

$$\nabla_{||}\Gamma_{||e} = \alpha_{sh}(x)\Gamma_{||e}\left(1 - n_{floor} / n\right) \qquad (1b)$$

where $\alpha_{sh}(x) = 2\rho_{sr}/L_{||}(x)$. The parallel connection length is a constant, $L_{||}(x)$ = 131 cm, in the present simulation. The substitution $\nabla_{||} \rightarrow 1/L_{||}$ reduces the model to two spatial dimensions. The parallel flux ($\Gamma_{||e}$) is given in Eq. (A6) of Ref. [7]. This is one of several 'closure' relations that provide analytical expressions for parallel fluxes or currents in terms of plasma parameters depending on the plasma regime (e.g., sheath or conduction limited). The factor $(1 - n_{floor} / n)$ in (1b) is necessary because the density is maintained above an imposed "floor" value (10^{12} cm^{-3}) for numerical expediency in the simulation. n_0 is the particle density moment of the neutral distribution function, G, evolved in Eq. (4a) below, and the ionization and recombination rate coefficients (h_{iz}, h_{rr}, and h_{3r}) are given in Eqs. (4d), (4e), and (4f).

Experimental values for the diffusion coefficient D_n,the thermal diffusivities $\chi_{e,i}$ and the viscosity μ discussed subsequently are, to our knowledge, poorly known in the divertor region. They are meant to account for processes not included in our model, such as neoclassical transport and micro-instabilities. The chosen values are consistent with those used in Ref. 7, and are similar, though slightly larger, that the effective diffusivities found near the separatrix for NSTX. [29]

The stationary source S_n models plasma streaming into the divertor region from the upstream scrape-off layer (SOL) and includes some leakage into the private-flux region (PFR); its shape is indicated in Fig. 2. The location of the maximum of $S_n(x)$ defines the separatrix ($\Delta x = 0$) in the simulation, and the maximum value there is $S_n(0) = 3.76\times10^{18}$ $cm^{-3}sec^{-1}$.

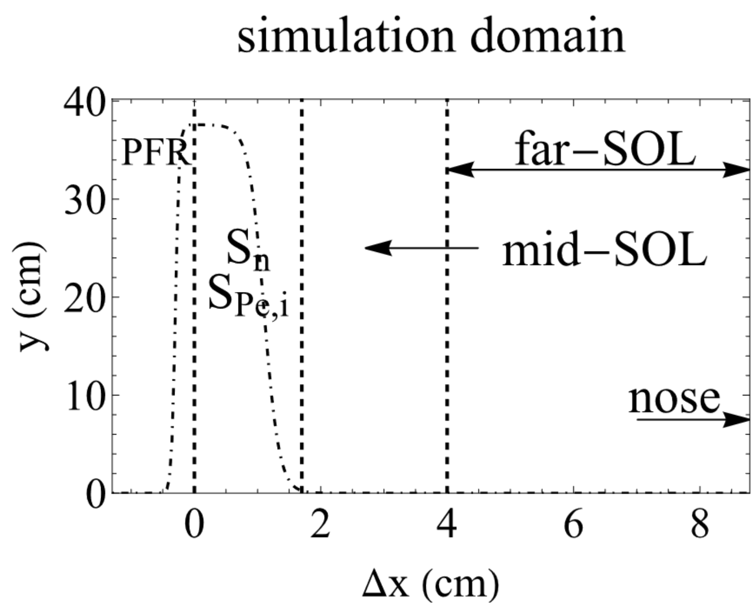

Fig. 2. The simulation domain includes (a) a private flux region (PFR, $\Delta x < 0$), (b) an upstream source region, concentrated on $-0.5 < \Delta x < 1.7$ cm, where the density source (S_n) and energy sources ($S_{Pe,i}$) are indicated qualitatively by the dot-dashed curve, (c) a mid-SOL region ($1.7 < \Delta x < 4$ cm), where turbulence-spreading is observed, and (d) the far-SOL ($4 < \Delta x < 8.8$ cm), bounded by the "nose" of divertor. [Associated dataset available at https://doi.org/10.5281/zenodo.7254770] (Ref. 39).

c. Plasma pressure

The electron and ion pressure evolution equations are, respectively,

$$\left[\partial_t \frac{3n}{2} T_e + \nabla\cdot(v_E \frac{3n}{2} T_e)\right] = \frac{3}{2} S_{P_e} + \nabla\cdot(\chi_e n \nabla T_e) - h_{iz} n_0 n\, E_{iz} - \nabla_{\|} Q_{\|e}$$
$$- \frac{3}{2} h_{rr} n^2 T_e + h_{3r} n^3 E_{iz0} - S_{n0} n E_{FC} \tag{2a}$$

and

$$\left[\partial_t \frac{3n}{2} T_i + \nabla\cdot(v_E \frac{3n}{2} T_i)\right] = \frac{3}{2} S_{P_i} + \nabla\cdot(\chi_i n \nabla T_i) - \nabla_{\|} Q_{\|i}$$
$$+(h_{iz} + h_{cx}) n_0 n\, E_0 - \frac{3}{2} h_{cx} n_0 n\, T_i \tag{2b}$$
$$- \frac{3}{2} h_{rr} n^2 T_i - \frac{3}{2} h_{3r} n^3 T_i \;.$$

S_{Pe} and S_{Pi} are stationary heating sources. The thermal diffusivities $\chi_{e,i}$ are constants equal to 30 m^2/sec. The parallel heat flux gradients, $\nabla_{\|} Q_{\|e,i}$, are given explicitly in Eqs. (A16) and (A17) of Ref. [7] and are similar in form to Eq. (1b). The ionization, charge-exchange and recombination rate coefficients (h_{cx} , h_{iz} h_{rr} , and h_{3r}) are given in Eqs. (4c), (4d), (4e), and (4f). n_0 and n_0E_0 are the neutral particle and energy density moments of the distribution function, G, evolved in Eq. (4a).

The stationary sources, S_{Pe} and S_{Pi}, model plasma streaming into the divertor region from the upstream scrape-off layer (SOL) and have the same shape as $S_n(x)$; they are indicated in Fig. 2. Their maximum values are $S_{Pe,i}(0)$ = 60 MW/m^3 in the simulation.

In Eq. (2a), E_{iz0} = 13.6 eV is the ionization energy and E_{iz} is the "ionization cost" responsible for cooling the electrons in the presence of neutrals. We take E_{iz} = 50 eV in the simulation. $S_{n0} = S_{n0}$ (x) is the source of Franck-Condon (FC) recycled neutrals, defined by Eq. (5a) below, and E_{FC} = 3 eV is the dissociation energy.[2,6]

d. Vorticity and the electrostatic potential

With the ion diamagnetic drift given by $\mathbf{v}_{di} = \mathbf{b} \times \nabla P_i$, the total ion fluid momentum density is $n(\mathbf{v}_E + \mathbf{v}_{di})$, and the component of its curl (i.e., the generalized vorticity) along $\mathbf{b}$ is

$$\mathbf{b}\cdot\nabla\times n(\mathbf{v}_E + \mathbf{v}_{di}) = n\nabla_\perp^2\phi + \nabla_\perp n\cdot\nabla_\perp\phi + \nabla_\perp^2 P_i \equiv -\rho \,. \tag{3a}$$

Given n, $P_i = nT_i$ and ρ, Eq. (3a) is solved for the electrostatic potential (ϕ) at each time step.

The evolution of ρ is as follows.

$$d_t\rho = -2b\times\kappa\cdot\nabla(P_e+P_i) - \left(\partial_x f_y - \partial_y f_x\right) - \nabla_{||}j_{||} + \mu\nabla^2\rho$$
$$+\frac{1}{2}\left[n_e v_{di}\cdot\nabla\nabla^2\phi\right] - \frac{1}{2}\left[v_E\cdot\nabla(\nabla^2 P_i) - \nabla^2(v_E\cdot\nabla P_i)\right] - \frac{1}{2}b\times\nabla n_e\cdot\nabla v_E^2 \tag{3b}$$

Here, $\boldsymbol{\kappa} = \mathbf{b}\cdot\nabla\mathbf{b} = -\mathbf{e}_x\rho_{sr}/R_m$ is the curvature vector ($\beta \equiv 2\rho_{sr}/R_m$ is the dimensionless curvature parameter.); μ is the coefficient of viscosity, taken to be constant at 30 m^2/sec; $\boldsymbol{f}$ is the neutral friction force density,

$$\boldsymbol{f} = h_{iz}n_0 n_e \mathbf{v}_0 + h_{cx}n_0 n_i\left(\mathbf{v}_0 - \mathbf{v}_E - \mathbf{v}_{di}\right)$$
$$-h_{rr}n_i n_e\left(\mathbf{v}_E + \mathbf{v}_{di}\right) - h_{3r}n_i n_e^2\left(\mathbf{v}_E + \mathbf{v}_{di}\right)\ , \tag{3c}$$

and $\mathbf{v}_0$ is the neutral fluid velocity. The radial component of $\mathbf{v}_0$ (v_{0x}) is given by the v_x-moment of the neutral distribution function, G, and the evolution of the bi-normal component (v_{0y}) is given in Eq. (4b) below. The parallel current gradient, $\nabla_{||}j_{||}$, is given in Eq. (A11) of Ref. [7].

e. Neutral distribution function

The evolution of the neutral species is described by the following equations.

$$\frac{\partial G}{\partial t} + v_x\frac{\partial G}{\partial x} = h_{cx}n_0 F_i - h_{cx}\bar{n}_i G - h_{iz}\bar{n}_e G$$
$$+h_{rr}\bar{n}_e F_i + h_{3r}\bar{n}_e^2 F_i + S_{n0} f_{FC} \tag{4a}$$

$$\partial_t v_{0y} = -v_{0x}\partial_x(v_{0y}) - \frac{1}{n_0}S_{n0}v_{0y}$$
$$+\left(h_{cx}\bar{n}_i + h_{rr}\frac{\bar{n}_i\bar{n}_e}{n_0} + h_{3r}\frac{n_i n_e^2}{n_0}\right)\left(\bar{v}_{Ey} + \bar{v}_{diy} - v_{0y}\right) \tag{4b}$$

Here $G = G(t,x,v_x)$ is the 1D neutral species distribution function, and $F_i = F_i(t,x,v_x)$ is a 1D Maxwellian distribution function based on the y-averaged ion density and temperature,

$$F_i = \bar{n}_i \exp\left[-v_x^2/(2\bar{T}_i)\right]/(2\pi\bar{T}_i)^{1/2}.$$

Only the y-averages of plasma fields, denoted by overbars (e.g., $\bar{n}_i$), appear in the evolution of G, and the plasma sees neutrals that are homogeneously distributed in y. If the 3D neutral distribution function is denoted by g, then $G(x,v_x,t) = \int dv_y dv_z \bar{g}$, and we have assumed no parallel (z) dependence. In Eqs. (4), $n_e = n_i \equiv n$; the distinction is purely to elucidate the underlying physical processes.

The form of the convective derivative in (4b) involves a closure ansatz for the $v_x v_y$-moment of $\bar{g}$. We indicate the result of that ansatz and the evolution of G, derived from the kinetic equation for g, and refer the reader to reference [6] for the derivations.

The charge exchange and ionization rate coefficients are similarly based on y-averaged electron and ion temperatures:

$$h_{cx}(\bar{T}_i) = 1.1\times10^{-14}\bar{T}_i(x,t)^{0.3}M_i^{-1/2} \;\; m^3/\mathrm{sec} \;\; \text{and} \tag{4c}$$

$$h_{iz}(\bar{T}_e) = 8\times10^{-15}\bar{T}_e(x,t)^{1/2}\exp\left[-13.56/\bar{T}_e(x,t)\right]/(1+0.01\bar{T}_e(x,t)) \;\; m^3/\mathrm{sec} \tag{4d}$$

where the temperatures are expressed in eV and M_i in AMU (M_i = 2 for D). These formulaic rates are fits to tabulated values of the collision rates that are used in kinetic neutral Monte Carlo simulations. [30] The recombination rate coefficients are similarly given in terms of the y-averaged electron temperature: [31]

$$h_{rr}(\bar{T}_e) = 5.2\times10^{-20}\left(\frac{E_{iz0}}{\bar{T}_e}\right)^{1/2}\left[0.43+\frac{1}{2}\ln(E_{iz0}/\bar{T}_e)+0.469(E_{iz0}/\bar{T}_e)^{-1/3}\right] \;\; m^3/\mathrm{sec} \tag{4e}$$

$$h_{3r}(\bar{T}_e) = 8.75\times10^{-39}\bar{T}_e^{-4.5} \;\; m^6/\mathrm{sec} \tag{4f}$$

Notice that h_{cx}, h_{iz}, and h_{rr} have the units of area times velocity, and are often denoted by "$\langle\sigma v\rangle_{cx}$" , etc., where σ represents the cross-section for the particular scattering process, while the 3-body rate coefficient, h_{3r}, has the units of σv/density. (Recombination is negligible in the present simulation where T_e is maintained above a floor of 1 eV for the sake of numerical stability.)

The charge-exchange and ionization rates have the units of inverse time and are given by the products of the neutral density with the respective rate coefficients, viz.,

$$\nu_{cx} = n_0 h_{cx} \tag{4g}$$

and

$$\nu_{iz} = n_0 h_{iz}\,. \tag{4h}$$

f. Neutral recycling

The source of neutrals, $S_{n0} f_{FC}$ in Eq. (4a), is provided by converting a fraction of the plasma parallel particle flux ($\Gamma_{||e}$) to neutral atoms assumed to originate in fully dissociated D_2 molecules:

$$S_{n0}(x) = R(x)\int_0^{L_x} dx \left\langle \nabla_{||}\Gamma_{||e} \right\rangle_y \tag{5a}$$

and

$$f_{FC}(v_x) = \exp[-(v_x - v_{D_2})^2 / 2T_{FC}] / (2\pi T_{FC})^{1/2} \,, \tag{5b}$$

where v_{D_2} is taken to be -0.8 km/sec, corresponding to room temperature (300° K) D_2 molecules, and T_{FC} is the Franck-Condon (FC) temperature, taken to be 3 eV. This is a time-dependent fueling source distributed throughout the simulation domain according to the profile function R(x), equal to A cos[(x-x_{sep})/(L_x-x_{sep}) π/2], with the coefficient A chosen so that the x-integral of R(x) is equal to a prescribed constant, R_0, the neutral recycling fraction. R_0 is equal to 1 in the simulation. Note that in the nSOLT model, the divertor target plate is at a distance $L_{||}$ out of (perpendicular to) the simulation plane: in this divertor simulation, neutral recycling from the target is therefore modeled everywhere in the (x,y) plane.

g. Boundary conditions

All plasma fields (n, T_e, T_i, ϕ) are periodic in y. The fluctuations in these fields (e.g., $\delta n = n - \bar{n}$) vanish at both radial (x) boundaries. The radial gradients of the density and temperatures are held to zero at x = 0 so that their diffusive fluxes vanish at that boundary. The mean potential ($\bar{\phi}$) is equal to 3 eV at the PFR boundary (x = 0), and its radial gradient ($\partial_x \bar{\phi} = \bar{v}_{Ey}$) is equal to zero at x = L_x; these boundary conditions are used to solve Eq. (3a) for the potential.

The distributions of neutrals that are leaving the simulation at the boundaries, i.e., G(x=0,v_x<0) and G(x=L_x, v_x>0), evolve solely by convection; these departing neutrals "free-stream" through the boundaries. Each departing neutral is replaced with an entering neutral with the opposite velocity, maintaining zero net particle flux at the boundaries. In other words, the neutrals are reflected at the boundaries:

$$G(x = L_x, v_x < 0) = G(x = L_x, v_x > 0) \text{ and } G(x = 0, v_x > 0) = G(x = 0, v_x < 0). \tag{6}$$

G is held to zero at the boundary of the velocity domain which extends to (±) $4c_s$ (280 km/sec), which is sufficient to contain the observed extent of G in the simulation.

h. Numerical methods

The overall updating of the plasma fields in nSOLT (n, T_e, T_i, ρ) is split-step: to each monomial term in the evolution equations there corresponds a subroutine that solves an initial value problem starting from the fields updated by the previous subroutine in the calling sequence of the main time loop. The algorithm used in the convection subroutine is flux-corrected transport (FCT) [32], chosen for its exceptional ability to resolve steep propagating fronts, e.g., blobs. The alternating-direction implicit (ADI) algorithm [33] is used to advance the fields by linear diffusion [i.e., terms proportional to D_n, $\chi_{e,i}$, and μ in Eqs. (1a), (2a, 2b), and (3b)]. The fields are updated explicitly by the parallel flux gradients ($\nabla_{||}\Gamma_{||e}$, $\nabla_{||}Q_{||e}$, $\nabla_{||}Q_{||i}$) and by the sources (S_n, S_{Pe}, S_{Pi}). The electrostatic potential (ϕ) is found by solving Eq. (3a) by the relaxation method of Angus and Umansky. [34]

The evolution of the neutral distribution function (G) is in three steps: free-streaming by upwind linear interpolation, CX update by a 2nd order Runge-Kutta method, and explicit updates for ionization and recombination. (The plasma fields are taken as fixed over a single time step, Δt.) The free-streaming update is constrained by $\max(|v_x|)\,\Delta t/\Delta x < 1$, where here v_x is the independent velocity variable of the neutral grid (x,v_x). With $\max(|v_x|) \sim c_s$ and $\Delta x \sim \rho_s$, this constraint amounts to $\Delta t < \Omega_i^{-1}$ which imposes no greater computational burden than required to maintain accuracy and stability, where $\Delta t \sim 10^{-2}\,\Omega_i^{-1}$ is typical in practice.

III. Ionization burst

a. Overview

Without neutrals in the simulation, the stationary sources (S_n, $S_{Pe,i}$) sustain a turbulent plasma equilibrium. The sudden introduction of neutral recycling causes a sharp rise in the plasma density and a sharp fall in the electron temperature. While the neutral density increases, this “burst” subsides, and a quiescent plasma state emerges; the plasma fields saturate while the neutral density continues to grow. Radial profiles of the plasma density and pressures are shown in Fig. 3 at three times: before neutral turn-on, at the peak of the burst, and at the end of the simulation after the burst has subsided. It can be seen from Fig. 3 that, at the peak of the burst, the density profile (red) has two local extrema, one at the separatrix ($\Delta x = 0$), where the density source S_n is maximized, and the other at $\Delta x = 1$ centimeter, which effectively shifts the overall profile farther out into the SOL compared to the source and compared to the pre-burst plasma profile (black). After the burst, the equilibrium density profile (green) is also shifted outward compared to the source and to the pre-burst equilibrium profile. It appears that the outward shifts of the burst profiles (red) are caused by the enhanced (blob) radial transport during the burst and that the shift seen in the post-burst profiles relative to both the pre-burst and burst profiles, is due to ionization. The green profiles lack the apparent skewness of the black and red curves that are likely due to blob transport. Instead, these approximately Gaussian equilibrium profiles are determined by balancing diffusion against sources including ionization and charge exchange in the wake of the burst.

We analyze the burst in detail to characterize the roles that neutral ionization and charge-exchange play in its evolution. It is hoped that the analysis of this particular event, in our numerical experiment, will prove useful in understanding the divertor environment at MAST-U and in general.

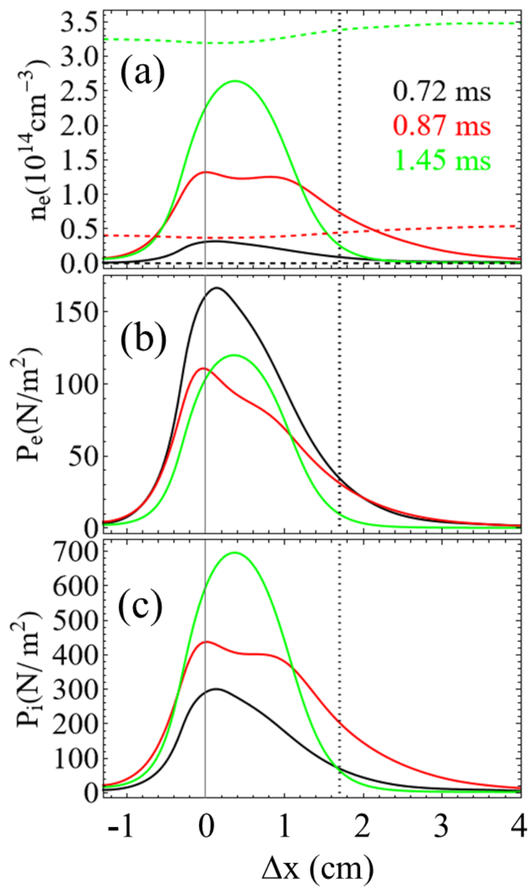

Fig. 3. Profiles of the plasma density (a), and of the electron (b) and ion (c) pressures at three times: before neutral turn-on (t = 0.72 ms, black curves), at the peak of the burst (0.87 ms, red curves), and at the end of the simulation (1.45 ms, green curves). The neutral density (n_0) profiles are shown in (a) as dashed curves at the same times. [Associated dataset available at https://doi.org/10.5281/zenodo.7254770] (Ref. 39).

During the burst, the radial plasma particle flux [$\Gamma_\perp = \langle \delta n \delta v_x \rangle$] increases 7-fold, compared to the pre-neutrals turbulent flux, but vanishes in the wake of the burst; the growing neutral density subsequently eliminates turbulent plasma perpendicular transport and reduces the parallel heat exhaust, particularly in the electron channel. See Fig. 4. Notice, however, that the plasma parallel particle flux, shown dashed in Fig. 4(b), is larger during and following the burst, than it is before the introduction of neutrals, to accommodate the ionization source.

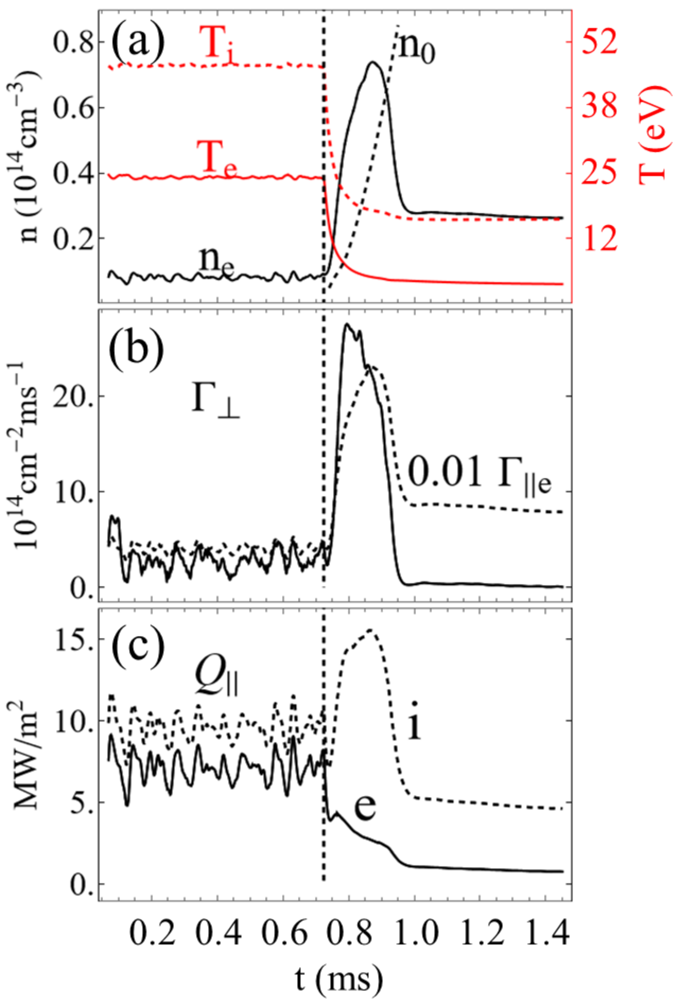

Fig. 4. Histories of the bi-normal (y) averages of (a) n_e, n_0, T_i, and T_e, (b) the turbulent particle perpendicular flux, $\Gamma_\perp = \langle \delta n \delta v_x \rangle$, and the electron parallel particle flux [$\Gamma_{||e}$, Eq. (A6), Ref. 7], times 0.01 (dashed), and (c) the electron and ion parallel heat fluxes [$Q_{||e,i}$, Eqs. (A16) and (A17), Ref. 7] at Δx = 1.7 cm (the average location of the maximum value of the interchange instability growth rate γ_{mhd}). The dashed vertical line indicates the time at which neutral recycling begins. [Associated dataset available at https://doi.org/10.5281/zenodo.7254770] (Ref. 39).

Although a recycling coefficient of unity was employed, causing the divergence of n_0, the plasma fields are apparently approaching equilibrium because the electron temperature has been reduced by ionization cost to the point where the ionization rate is small. [With reference to Eqs. (4d) and (4h), h_{iz} goes to zero exponentially fast as T_e drops below the ionization potential (13.56 eV) and it does so faster than the neutral density grows so that the ionization rate, ν_{iz} = $n_0 h_{iz}$, approaches zero.] In fact, from Fig. 4(a) it is seen that once n_0 surpasses the plasma density n_e, following the burst (i.e., t > 1.0 ms), the plasma evolution is nearing saturation. The charge exchange rate, Eqs. (4c) and (4g), does continue to grow with n_0; however, this forces T_i

to approach 2/3 E_0 in the emerging equilibrium, and the ions cease to be cooled by charge exchange; see Eq. (2b).

The remainder of Sec. III is organized into four parts: In (b), we compare the measured fluctuation growth rate ($\nu_{\delta n}$), the interchange instability growth rate (γ_{mhd}), and the CX damping rate (ν_{CX}), together with the spatially averaged E×B flow shearing rate, $\partial_x v_{Ey} \equiv \xi$, from the burst. A linear dispersion relation guides interpretation of these measurements. In (c), an expression for the equilibrium shearing rate is derived that enables comparison between ν_{CX} and characteristic sheath frequencies in determining the shearing rate. In (d), we show that the increase in collisionality at the onset of the burst disconnects blob filaments from the divertor sheath. Finally, in (e), CX friction, acting on the ion diamagnetic drift in the vorticity equation, is shown to overtake the curvature force, turning off the turbulent particle flux at the end of the burst.

b. Ionization cooling, charge-exchange damping, and a local linear dispersion relation

The CX rate ($\nu_{CX} = h_{CX} n_0$), the interchange growth rate ($\gamma_{mhd} = c_s / (RL_p)^{1/2}$), and the shearing rate of the mean E×B flow ($\partial_x v_{Ey}$) are plotted in Fig. 5(a). Here $1/L_p = -(\partial/\partial x) \ln P$ defines the pressure gradient scale length. The IZ rate, $\nu_{iz} = h_{iz} n_0$, and the growth rate of the plasma density fluctuation, $\nu_{\delta n} = (d/dt)\ln(\delta n)_{r.m.s.}$, where $\delta n_{r.m.s.} = \langle \delta n^2 \rangle_y^{1/2}$ are plotted in Fig. 5(b). These rates are measured at the time-averaged radial (x) location of the maximum value of γ_{mhd} , which is at Δx = 1.7 cm in both the pre- and post-neutrals phases of the simulation. The magnitude of the shearing rate is averaged over a 20 μs window ending at time t. Averaging the shearing rate removes high frequencies that would obscure the comparison in Fig. 5(a); the plasma pressure profile is comparatively quiet.

With the onset of neutral recycling and ionization, the plasma grows denser and colder. The burst begins with neutral turn-on at t = 0.72 ms and lasts until about t = 0.9 ms, during which time T_e falls from 24 eV to 3 eV at the reference location (Δx = 1.7 cm), and n_e rises from 1×10^{13} cm^{-3} to 7×10^{13} cm^{-3}. See Fig. 4(a). During the burst, γ_{mhd} decreases from 1.5 to 0.7 μs^{-1}, due to ionization cooling of the electrons and CX cooling of the ions. A drop in the shearing rate is observed and will be attributed to the drop in T_e, later in the paper [Sec. III(c)].

Early in the burst, the growth rate of the density fluctuations ($\nu_{\delta n}$) increases to a maximum of 0.04 μs^{-1}. See Fig. 5(b). At this maximum and until t = 0.8 ms, the growth rate is approximately equal to ν_{iz}, which is seen to be decreasing as T_e decreases. Both the mean plasma density and the density fluctuation grow at the ionization rate, preserving $\delta n/n$ during the burst, and subsequently decay. A local linear dispersion relation enables further analysis of the burst.

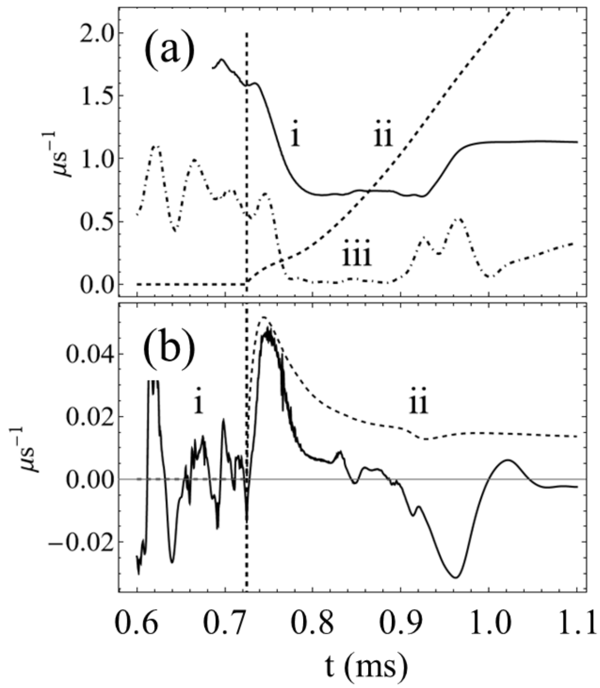

Fig. 5. (a) Histories of (i) the growth rate of the "bare" interchange instability, $\gamma_{mhd} = c_s / (RL_p)^{1/2}$ (solid), (ii) the charge exchange damping rate, ν_{cx} (dashed), and (iii) the magnitude of the flow shearing rate, $\xi = \partial_x v_{Ey}$, averaged over a 20 μs window (dot-dashed). (b) Histories of (i) the growth rate of the density fluctuation $\nu_{\delta n} = (d/dt)\ln(\delta n)_{r.m.s.}$ (solid), and (ii) the ionization rate ν_{iz} (dashed). The dashed vertical line indicates the time at which neutral recycling begins. [Associated dataset available at https://doi.org/10.5281/zenodo.7254770] (Ref. 39).

A local, linear dispersion relation (LDR) is derived from a reduced set of the model equations in Appendix A:

$$\left(\omega - \omega_E + i\hat{\nu}_{cx}\right)\left(\omega - \omega_E - \omega_{*i}\right) = -\gamma_{mhd}^2 - i(\omega - \omega_E)\omega_S \,, \tag{7a}$$

where the subscripted quantities in (7a) are given above and in the appendix. In particular, ω_E is the Doppler shift from the **E**×**B** drift, ω_{*i} is the ion diamagnetic frequency, and the loss of charge due to the parallel current is represented by the sheath frequency,

$$\omega_S = \frac{c_S}{L_{||}k^2\rho_s^2}\frac{\omega}{\tilde{\omega}}\left(1+\hat{\Lambda}\right)^{-1} \rightarrow \frac{\hat{\sigma}_S}{k^2 n L_{||}^2}\left(1+\hat{\Lambda}\right)^{-1}, \tag{7b}$$

with

$$\hat{\Lambda} \equiv \sigma_S / \sigma_C = 0.51(1+T_i / T_e)^{1/2}\frac{\omega}{\tilde{\omega}}\Lambda \,, \tag{7c}$$

and $$\Lambda \equiv \frac{\nu_{ei} L_{\|}}{\Omega_e \rho_{sr}}. \tag{7d}$$

$\hat{\Lambda}$ is the ratio of sheath to collisional conductivities, $\hat{\Lambda} = \sigma_S / \sigma_C$, and Λ is the blob collisionality parameter.[9] In Eq. (7b), the first form expresses ω_S in terms of dimensional quantities, and the second term gives it in terms of dimensionless quantities, where the dimensionless sheath conductivity, $\hat{\sigma}_S$, is given by Eq. (A22). The plasma fields (n, $P_{e,i}$, $T_{e,i}$) are represented by their bi-normal (y) averages, and the frequency in the plasma rest frame is $\tilde{\omega} = \omega - \omega_E$.

Equation (7a) will be recognized as containing the minimal physics required to describe interchange instability as well as the so-called conducting-wall mode or ∇T_e sheath instability.[35] Formally replacing $\omega/\tilde{\omega}$ with unity in Eqs. (7b) and (7c) corresponds to the neglect of electron temperature fluctuations in deriving the dispersion relation: for simplicity this is done in the remainder of this section. In this case, ω_S is independent of frequency. For the parameters of the present simulation, the interchange drive dominates over the conducting-wall drive, (for which electron temperature fluctuations are essential) but the sheath term is nevertheless important, as described next.

All of the subscripted quantities in (7a) depend on the wave numbers (k_x, k_y). We solved the LDR (7a) for ω using $k_x = 0$ and $k_y = 1.40$ cm^{-1}. This choice of k_y maximizes the energy spectrum of the density fluctuations at $\Delta x = 1.7$ cm in the simulation at all times leading up to and including the burst and corresponds to the mean poloidal spacing between blob filaments. The choice of $k_x = 0$ corresponds to a long radial filament (i.e., long relative to the bi-normal scale of the structure) or "streamer." (It is true that fully formed blobs have a finite radial structure. However, the so-called blob dispersion relation, obtained with $k_x = 0$ and $k_\perp \sim k_y \sim 1/\delta_b$ where δ_b is the blob radius, captures the qualitative features of blob dynamics surprisingly well. See for example Ref. 9, Sec. V.2 "Blob correspondence principle.")

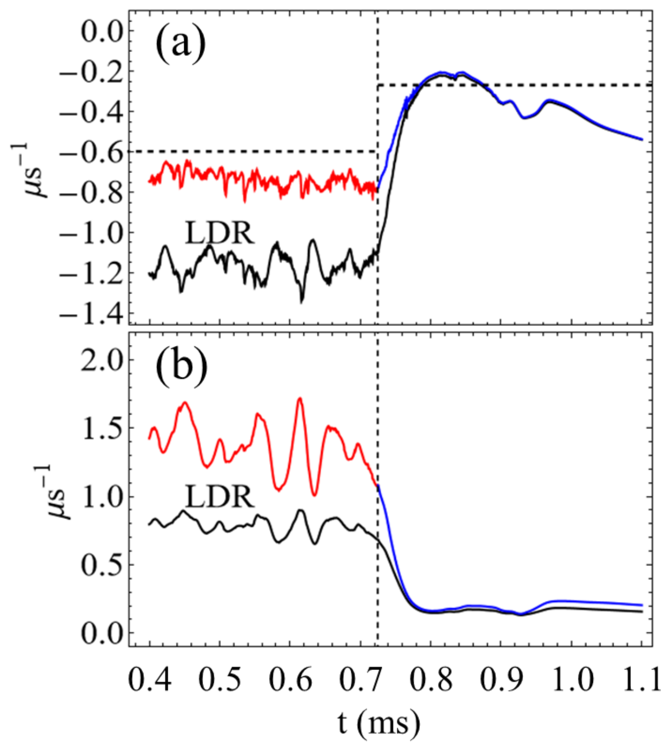

Fig. 6. (a) Real and (b) imaginary parts of the frequency predicted by the local dispersion relation (LDR), Eq. (7a), for the mean fields from the simulation, measured at $\Delta x = 1.7$ cm. The wave numbers were taken to be $k_x = 0$ and $k_y = 1.40\ \mathrm{cm}^{-1}$. Approximations (8a) and (8b) are plotted in red and blue, respectively. The dashed horizontal lines in (a) indicate the dominant mode found in the power spectrum of the density fluctuations at $\Delta x = 1.7$ cm. The dashed vertical line indicates the time at which neutral recycling begins. [Associated dataset available at https://doi.org/10.5281/zenodo.7254770] (Ref. 39).

Prior to neutral recycling ($\nu_{cx} = 0$), the LDR has an unstable mode at $\omega_R = -1.2\ \mu s^{-1}$, on time-average, corresponding to a phase velocity of $\omega_R/k_y = -0.86$ cm/μs. See Fig. 6. This phase velocity is two times the simulation value, –0.43 cm/μs, measured from the power spectrum of the density fluctuations. The LDR growth rate is $\omega_I = 0.75\ \mu s^{-1}$ which is better approximated by $\gamma_{\rm mhd}^2/\omega_S$ (1.0 μs^{-1}) than by $\gamma_{\rm mhd}$ (1.7 μs^{-1}). So, the LDR mode may be described approximately as a sheath-moderated interchange mode,[36] i.e., the solution of (7a) in the limits $\omega_S >> \gamma_{\rm mhd}$ and $\omega_S >> |\omega_{*i}|$, viz.,

$$\omega \to \omega_E + i\gamma_{\rm mhd}^2/\omega_S\,. \tag{8a}$$

From Eq. (7b), it is apparent that plasmas of low collisionality are more likely to support this mode than are plasmas of high collisionality where ω_S is small and electrical connection to the divertor target is lost. Finally, it is worth noting that the phase velocity of the fluctuations in Eq.

(8a) is reduced from v_E to zero if δT_e fluctuations are retained in the simple advective limit of Eq. (A8.1). Thus, an intermediate response of δT_e, which appears to be more representative of the simulation, would bring the LDR-predicted phase velocity into better agreement with the simulation value.

In the high (Coulomb) collisionality limit, with $\nu_{cx} = 0$, one theoretically recovers the interchange mode at $\omega = i\gamma_{mhd}$. During the burst, as the plasma density increases from ionization, and the electron temperature decreases, the collisionality does increase dramatically. However, the interchange limit is not observed, i.e., the observed growth rates do not increase. Instead, as described next, ν_{cx} dominates the dispersion relation. This is likely related to the fact that the charge exchange cross-section is larger than the ionization cross-section.

From the onset of neutral recycling, ν_{cx} grows roughly linearly with time, eventually surpassing all of the other subscripted rates in (7a). In the limit $\nu_{CX} >> |\omega - \omega_E|$, γ_{mhd}, ω_s we find

$$\omega \to \omega_E + \frac{\omega_{*i} + i\gamma_{mhd}^2/\hat{\nu}_{CX}}{1 + \omega_S/\hat{\nu}_{CX}}. \qquad (8b)$$

The phase velocity approaches $v_E + v_{di}$, and CX damping directly mitigates the interchange instability, potentially eliminating it by acting in combination with other stabilizing mechanisms (e.g., diffusion) not included in (7a). There is evidence for this limiting behavior in the burst.

After the onset of neutral recycling, the power spectrum of the density fluctuations in the simulation is dominated by the burst, as the energy in the fluctuations decreases rapidly thereafter. That spectrum indicates a phase velocity of –0.19 cm/μs (ω_R = –0.27 μs^{-1}), increased from the pre-neutrals value of –0.43 cm/μs (ω_R = –0.6 μs^{-1}). The LDR prediction and the limit (8b) are in good agreement and predict a slowly changing frequency in a neighborhood of the simulation result. See Fig. 6(a).

During the burst, v_E increases from its pre-burst value of –0.5 cm/μs to –0.1 cm/μs. This decrease in *magnitude* is initially due to the reduction in ϕ_B ($3T_e$) caused by ionization cooling, while the plasma remains connected to the sheath, and continues after the burst due to the growing neutral friction drag. As a result, ω_{*i} dominates the dispersion of plane waves in the aftermath of the burst.

Later in the paper, Sec. III(e), the radial propagation of blobs during and after the burst is investigated. The blob velocity v_b is qualitatively related to the growth rate from linear theory, $v_b \sim \omega_I / k_y$, according to the correspondence principle.[9] We digress to investigate that here. As ν_{cx} increases and the electrons cool, ω_s becomes negligible and, neglecting ω_E as just discussed, (8b) is approximately

$$\omega = \omega_{*i} + \frac{i\gamma_{mhd}^2}{\hat{\nu}_{CX}}. \quad (8c)$$

The condition for $\omega_R > \omega_I$ is therefore, reverting to dimensional units with $k_x = 0$, $\omega_{*i}\nu_{CX} > \gamma_{mhd}^2$. Noting that $\gamma_{mhd}^2 \sim 2c_s^2/(RL_p)$ and for $c_s \sim v_{ti}$, $\omega_{*i} \sim k_y c_s \rho_s / L_p$ one obtains

$$\nu_{cx} > \frac{2\Omega_i}{k_y R}. \quad (8d)$$

as a rough condition for the frequency to be dominantly real. In dimensionless variables this condition is just $\beta < k_y \nu_{cx}$, where $\beta = 2\rho_{sr}/R$ is the normalized curvature parameter. We will see that this defines a critical blob size $a_{DQ} \sim \nu_{cx}/\beta$. Larger blobs will be dominated by the usual interchange forces in γ_{mhd} and propagate radially, smaller blobs, with ω real, will have an incorrect phase relationship between δn and $\delta\phi$ for radial propagation. This will be explored in more detail in Sec. III(e).

c. Neutral effects on mean E×B flow

A radially sheared **E**×**B** flow can moderate the interchange instability or provide a barrier to radial transport.[37] In either case, a reduction in the shearing rate caused by the onset of CX damping might be responsible for the burst of turbulent flux, as seen in other works.[2,3] We derive an expression for the shearing rate in equilibrium that allows us to explore this possibility.

In equilibrium ($\partial_t = 0$) and in the limit of cold ions ($P_i = 0$), an equation may be obtained from the poloidal (y) average of Eq. (3b):

$$\begin{aligned} &-\partial_x\left[\left\langle \delta n \delta v_x \right\rangle \partial_x \bar{v}_y + \bar{n}\,\partial_x \left\langle \delta v_x \delta v_y \right\rangle\right] - \partial_x \left\langle \nu_{cx} n v_y \right\rangle \\ &+\left\{ \alpha_{sh}\left\langle n c_s\left(\phi-\phi_B\right)/T_e\right\rangle,\ \alpha_{sh}\left\langle 1.96\frac{\Omega_e}{\nu_{ei0}} T_e^{3/2}\left(\phi-\phi_B\right)/L_{\|}\right\rangle\right\} = 0. \end{aligned} \quad (9a)$$

(We use the cold ion approximation here for simplicity, despite the fact that the local ion pressure gradient is competitive with that of the electrostatic potential.) In Eq. (9a), both the overbar and angular bracket denote the y-average, and we have replaced $\left\langle \nabla_{\|} j_{\|}\right\rangle$ by a choice between the sheath-limited (SL) and collision-limited (CL) forms, viz., $\alpha_{sh}\left\langle n c_s\left(\phi-\phi_B\right)/T_e\right\rangle$ and $\alpha_{sh}\left\langle 1.96\frac{\Omega_e}{\nu_{ei0}} T_e^{3/2}\left(\phi-\phi_B\right)/L_{\|}\right\rangle$, respectively, within braces. The smaller of the two in absolute value is the one that is applicable. This is a jump-discontinuous approximation to the Padé expression used in the nSOLT model.[7] We have also made the Boussinesq approximation by ignoring the density gradient in the expression for the generalized vorticity, but the fluctuating density is retained.

Integrated over x, and to lowest order in the fluctuations, Eq. (9a) becomes

$$
\begin{aligned}
&-\left[\left\langle \delta \mathrm{n} \delta \mathrm{v_x} \right\rangle \bar{\mathrm{v}}_{\mathrm{y}}' + \bar{\mathrm{n}}\, \partial_{\mathrm{x}} \left\langle \delta \mathrm{v_x} \delta \mathrm{v_y} \right\rangle\right] - \nu_{\mathrm{cx}} \bar{\mathrm{n}} \bar{\mathrm{v}}_{\mathrm{y}} \\
&+\int^{x} dx \left\{ \alpha_{\mathrm{sh}} \bar{\mathrm{n}} \bar{\mathrm{c}}_{\mathrm{s}} \left(\bar{\phi} - \bar{\phi}_{\mathrm{B}}\right) / \bar{\mathrm{T}}_{\mathrm{e}},\ \alpha_{\mathrm{sh}} 1.96 \frac{\Omega_{\mathrm{e}}}{\nu_{\mathrm{ei0}}} \bar{\mathrm{T}}_{\mathrm{e}}^{3/2} \left(\bar{\phi} - \bar{\phi}_{\mathrm{B}}\right) / \mathrm{L}_{\|} \right\} = 0,
\end{aligned}
\tag{9b}
$$

where the prime denotes differentiation with respect to x. Defining the potential gradient scale length (L_ϕ) by $\bar{\mathrm{v}}_{\mathrm{y}} = \bar{\phi}' \equiv \bar{\phi} / \mathrm{L}_\phi$, the flow shearing rate is given by $\bar{\mathrm{v}}_{\mathrm{y}}' = \bar{\phi} / \mathrm{L}_\phi^2$. Replacing $\bar{\phi}$ with $\bar{\mathrm{v}}_{\mathrm{y}}' \mathrm{L}_\phi^2$ and $\bar{\mathrm{v}}_{\mathrm{y}}$ with $\bar{\mathrm{v}}_{\mathrm{y}}' \mathrm{L}_\phi$, and assuming that the integrands in (9b) are approximately constant on domains of length L_ϕ, we obtain

$$
\begin{aligned}
&-\left\langle \delta \mathrm{n} \delta \mathrm{v_x} \right\rangle \bar{\mathrm{v}}_{\mathrm{y}}' - \bar{\mathrm{n}}\, \partial_{\mathrm{x}} \left\langle \delta \mathrm{v_x} \delta \mathrm{v_y} \right\rangle - \nu_{\mathrm{cx}} \bar{\mathrm{n}} \mathrm{L}_\phi \bar{\mathrm{v}}_{\mathrm{y}}' \\
&+\left\{ \mathrm{L}_\phi \alpha_{\mathrm{sh}} \bar{\mathrm{n}}\, \bar{\mathrm{c}}_{\mathrm{s}} \left(\bar{\mathrm{v}}_{\mathrm{y}}' \mathrm{L}_\phi^2 - \bar{\phi}_{\mathrm{B}}\right) / \bar{\mathrm{T}}_{\mathrm{e}},\ \mathrm{L}_\phi \alpha_{\mathrm{sh}} 1.96 \frac{\Omega_{\mathrm{e}}}{\nu_{\mathrm{ei0}}} \bar{\mathrm{T}}_{\mathrm{e}}^{3/2} \left(\bar{\mathrm{v}}_{\mathrm{y}}' \mathrm{L}_\phi^2 - \bar{\phi}_{\mathrm{B}}\right) / \mathrm{L}_{\|} \right\} = 0.
\end{aligned}
\tag{9c}
$$

Solving (9c) for the shearing rate, we find

$$
\bar{\mathrm{v}}_{\mathrm{y}}' = \frac{\partial_{\mathrm{x}} \left\langle \delta \mathrm{v_x} \delta \mathrm{v_y} \right\rangle / \mathrm{L}_\phi + \alpha_{\mathrm{sh}} \bar{\phi}_{\mathrm{B}} \left\{ \bar{\mathrm{c}}_{\mathrm{s}} / \bar{\mathrm{T}}_{\mathrm{e}},\ 1.96 \frac{\Omega_{\mathrm{e}}}{\nu_{\mathrm{ei0}}} \frac{\bar{\mathrm{T}}_{\mathrm{e}}^{3/2}}{\bar{\mathrm{n}} \mathrm{L}_{\|}} \right\}}{\left[-\left\langle \delta \mathrm{n} \delta \mathrm{v_x} \right\rangle / \bar{\mathrm{n}} \mathrm{L}_\phi - \nu_{\mathrm{cx}} + \alpha_{\mathrm{sh}} \mathrm{L}_\phi^2 \left\{ \bar{\mathrm{c}}_{\mathrm{s}} / \bar{\mathrm{T}}_{\mathrm{e}},\ 1.96 \frac{\Omega_{\mathrm{e}}}{\nu_{\mathrm{ei0}}} \frac{\bar{\mathrm{T}}_{\mathrm{e}}^{3/2}}{\bar{\mathrm{n}} \mathrm{L}_{\|}} \right\} \right]}. \tag{10}
$$

Equation (10) suggests that charge exchange damping (ν_{cx}) mitigates sheared flow driven by the gradient of the Reynolds stress, $\partial_{\mathrm{x}} \left\langle \delta \mathrm{v_x} \delta \mathrm{v_y} \right\rangle$. If the pre-neutrals turbulence were driven by interchange instability moderated by sheared flow, or if the sheared flow were providing a transport barrier, then the introduction of neutrals could cause a burst of turbulence by reducing the shearing rate. Then, with growing ν_{cx}, the interchange instability growth rate would be reduced, c.f., Eq. (8b), and the recently unleashed turbulence would subside. This scenario is qualitatively consistent with the observed burst but does not appear to be at work in the simulation.

As seen in Fig. 5(a), the shearing rate is significantly less than γ_{mhd} at all times, and it is doubtful that it is moderating the interchange-driven turbulence, either before or after the onset of neutral recycling. (A comparison of fluctuation scale lengths to pressure profile scale lengths suggests that profile gradient modification, i.e., the mixing length estimate with $\delta n/n \sim 1$, is the saturation mechanism in the pre-neutrals phase of the simulation.) Nor is a sudden drop in the shearing rate observed just before or immediately upon neutral recycling; the averaged shearing rate of Fig. 5(a) actually increases at the start of the burst. In fact, for the parameters of the simulation, CX damping is negligible in determining the equilibrium flow in comparison with sheath physics.

The individual expressions appearing in Eq. (10) were calculated from the simulation and their root-mean-square (rms) values, taken over the SOL ($\Delta x > 0$) at each instant of time, were compared. [For example, rms($\bar{\phi}$) is defined as $\mathrm{rms}(\bar{\phi}) = \left\langle (\bar{\phi})^2 \right\rangle_{\Delta x > 0}^{1/2}$. Note that this is a radial (x) average of the over-barred, i.e., y-averaged, field $\bar{\phi}$.] The scale length squared (L_ϕ^2) was taken to be the ratio rms($\bar{\phi}$) / rms($\bar{v}_y'$) from the simulation. It was found that the terms proportional to α_{sh} in Eq. (10), i.e., the parallel current terms, dominate all other terms before and after the onset of neutral recycling. [For example, in the pre-neutrals phase of the simulation the current is sheath-limited; the rms first (SL) term in curly brackets in the numerator is 6.3±0.2 μs^{-2} and is *smaller* than the rms second (CL) term, 150±20 μs^{-2}, and both dwarf the rms Reynolds term, 0.035±0.01 μs^{-2}.] It follows that, on average in the SOL, a good approximation to Eq. (10) is

$$\bar{v}_y' = \frac{\bar{\phi}_B}{L_\phi^2} = \frac{3\bar{T}_e}{L_\phi^2}. \tag{11}$$

In other words, the shearing rate is just the second derivative of the equilibrium sheath potential. The dominance of sheath or collisional physics over charge exchange in determining the shearing rate is due in part to the short connection length to the divertor target for the simulation plane considered here. The rms average of Eq. (11) is compared to the rms shearing rate from the simulation in Fig. 7. We note that L_ϕ^2 decreases from 1.8±0.2 cm^2 to 0.5 cm^2 upon neutral recycling while rms($\bar{T}_e$) falls from 1.5 to 0.2 eV in the SOL, accounting for the reduction in $\bar{v}_y'$ by about one half according to Eq. (11) and seen in Fig. 7.

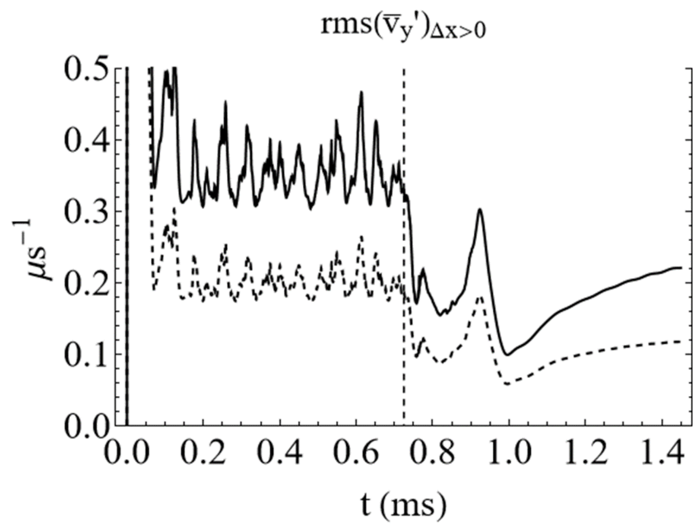

Fig. 7. The root-mean-square (rms) E×B flow shearing rate in the SOL from the simulation (solid) and predicted by Eq. (11) (dashed). [Associated dataset available at https://doi.org/10.5281/zenodo.7254770] (Ref. 39).

Thus, ionization cooling of the electrons dominates the observed reduction in **E**×**B** flow shearing following the onset of neutral recycling. The corresponding increase in collisionality disconnects the plasma filaments from the sheath, as we discuss next.

d. Disconnection by ionization cooling

At the onset of neutral recycling, ionization decreases the electron temperature and increases the plasma density, and so the collision frequency, $\nu_{ei} \sim n_e / T_e^{3/2}$, increases. In the limit that the parallel collisional resistivity ($1/\sigma_C$) is much greater than sheath resistivity ($1/\sigma_S$), the plasma blob filaments are insulated, or disconnected, from the sheath. The ratio of conductivities, $\hat{\Lambda} = \sigma_S / \sigma_C$, c.f. Eq. (7c), serves as a disconnection parameter. In the limit of infinite $\hat{\Lambda}$, the sheath frequency (ω_S) vanishes from the LDR, Eq. (7a), suggesting a change in blob dynamics with disconnection. For example, it has been shown that disconnected blobs propagate radially faster than connected blobs,[9] in the absence of neutral interactions.

The y-averaged disconnection parameter at the reference location (Δx = 1.7 cm) is plotted in Fig. 8. (We set $\omega / \tilde{\omega} \rightarrow 1$ in Eq. (7c) and plot the result, which is independent of frequency, in Fig. 8 for simplicity, formally ignoring the effect of temperature fluctuations in the LDR.) The plasma is sheath-connected prior to the onset of neutral recycling and is disconnected by the burst, and it remains disconnected following the burst. In Fig. 9, snap shots of the disconnection parameter in 2D are compared with snap shots of the normalized density fluctuations, at times before and after the onset of neutral recycling. It is seen that at the earlier time, Fig. 9 (a and b), the larger blob fluctuations ($\delta n_e / \bar{n}_e > 1$) have $\sigma_S / \sigma_C < 1$ and are, therefore, sheath-connected. At the later time, Fig. 9 (c and d), but before peak disconnection is observed at Δx = 1.7 cm (Fig. 8), the larger blob fluctuations have $\sigma_S / \sigma_C > 1$ and are disconnected.

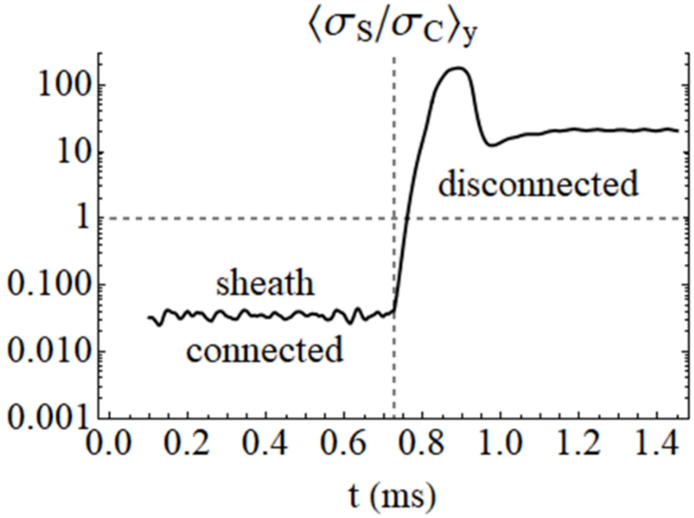

Fig. 8. History of the y-averaged ratio of sheath to collisional conductivities, σ_S/σ_C, [Eq. (7c) with $\omega/\tilde{\omega} \to 1$], at the reference location (Δx = 1.7 cm). Values (less, greater) than one indicate that (sheath physics, collisionality) is limiting the parallel current. [Associated dataset available at https://doi.org/10.5281/zenodo.7254770] (Ref. 39).

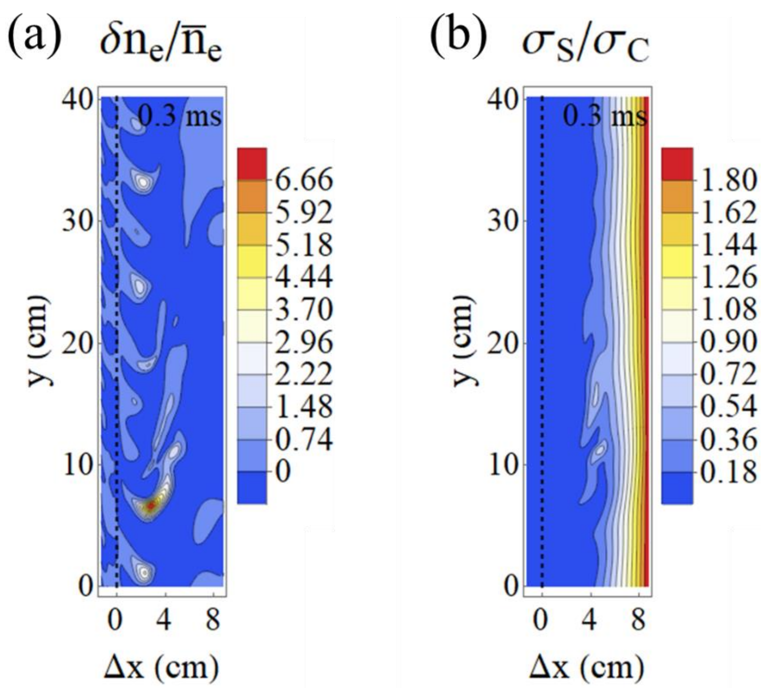

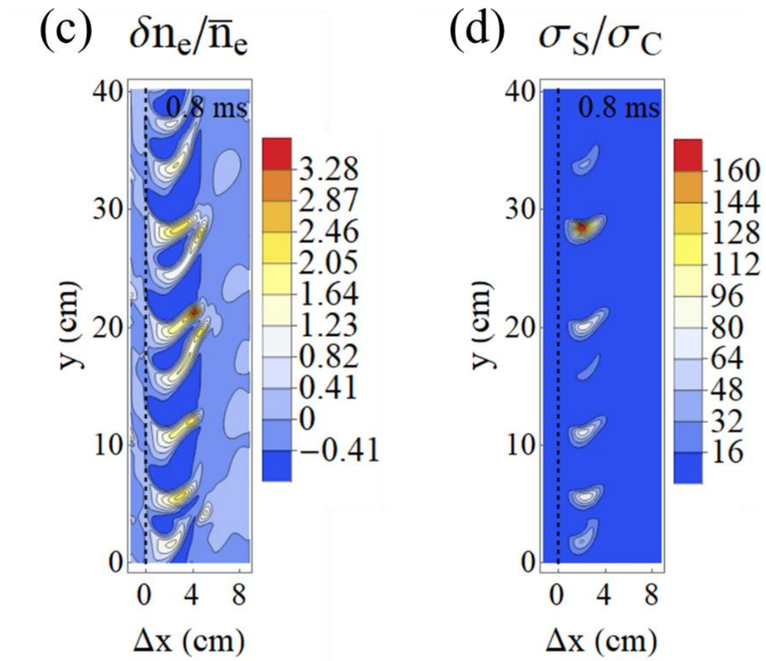

Fig. 9. (a) Normalized density fluctuation, $\delta n_e / \bar{n}_e$, and (b) disconnection ratio, σ_S/σ_C [Eq. (7c) with $\omega / \tilde{\omega} \rightarrow 1$] at t = 0.3 ms, before the start of neutral recycling: Blobs ($\delta n_e / \bar{n}_e > 1$) are sheath-connected ($\sigma_S/\sigma_C < 1$). (c) and (d): As in (a) and (b), respectively, but at t = 0.8 ms, after neutral turn-on: Blobs are disconnected ($\sigma_S/\sigma_C > 1$) from the sheath by collisionality. Note the difference in palette scales. [Associated dataset available at https://doi.org/10.5281/zenodo.7254770] (Ref. 39).

As mentioned above, disconnected blobs are expected to move faster radially than connected blobs, absent neutral interactions. Indeed, the radial particle flux ($\Gamma_\perp$) increases dramatically following the onset of recycling. However, this transport burst is dominated by the initial increase in the plasma density due to ionization, and the flux subsequently falls to zero in the wake of the burst. See Fig. 4.

As discussed in Sec. III(b) above, the combination of disconnection ($\omega_s \rightarrow 0$), driven by increased collisionality, and growing charge-exchange damping ($\nu_{cx} \rightarrow \infty$), leads to a transition from interchange-dominated dispersion ($\omega^2 \sim -\gamma_{mhd}{}^2$) to a purely real frequency mode ($\omega \sim \omega_{*i}$). According to the blob correspondence principle, this implies a transition from radially propagating blobs ($v_b \sim \omega_I/k_y$) to non-propagating blobs, i.e., to blob stagnation, and could account for the observed loss of turbulent transport in the wake of the burst. We explore this picture with spatially-localized (blob) diagnostics in the next section.

e. Blob stagnation by CX friction

The equation of vorticity evolution (3b) is the curl of the ion momentum density evolution equation in which the x-component of the neutral friction force $\boldsymbol{f}$, Eq. (3c), is seen to compete with the x-directed curvature force, $\boldsymbol{\kappa}(P_e + P_i)$. Translated into the vorticity evolution equation, that competition is between $-\partial_y f_x$ and $-2\mathrm{b}\times\boldsymbol{\kappa}\cdot\nabla(P_e + P_i)$. In particular, we focus on the charge-exchange component of $-\partial_y f_x$, i.e., $\partial_y \nu_{cx} n_i v_{di,\,x} = -\nu_{cx}\partial_y^2 P_i$, which is proportional to the second derivative of the ion pressure. The curvature drive, $-2\mathrm{b}\times\boldsymbol{\kappa}\cdot\nabla(P_e + P_i) = \beta\partial_y(P_e + P_i)$, on the other hand, is proportional to the first derivative of the total pressure and, acting on a localized fluctuation (blob or streamer), drives the bi-normal (y) dipole charge fluctuation that is responsible for radial blob propagation.[9] The CX force, acting alone on a blob, would tend to drive a tripole charge fluctuation in the y direction resulting in no net radial propagation. In fact, the E×B velocity field inferred for such a charge distribution would tend to tear the blob in half with the top and bottom (in y) portions moving in opposite directions. The smaller structures resulting from a repetition of this process will dissipate.

In addition, the central portion of the blob with its monopole field causes rotation (spin) of the charge dipole. This nonlinear effect converts radial motion into poloidal motion, and at sufficiently large rotations, causes charge mixing. See the discussion of blob spin in Refs. [8] and [9]. These effects reduce the usual dipole-induced radial motion of the blob. Thus, even though the dipole effect is still present, once the tripole effect is competitive, radial motion begins to be suppressed. As discussed in Sec. III(b), suppression of the dipole charge itself occurs when $\nu_{cx} > \gamma_{mhd}$.

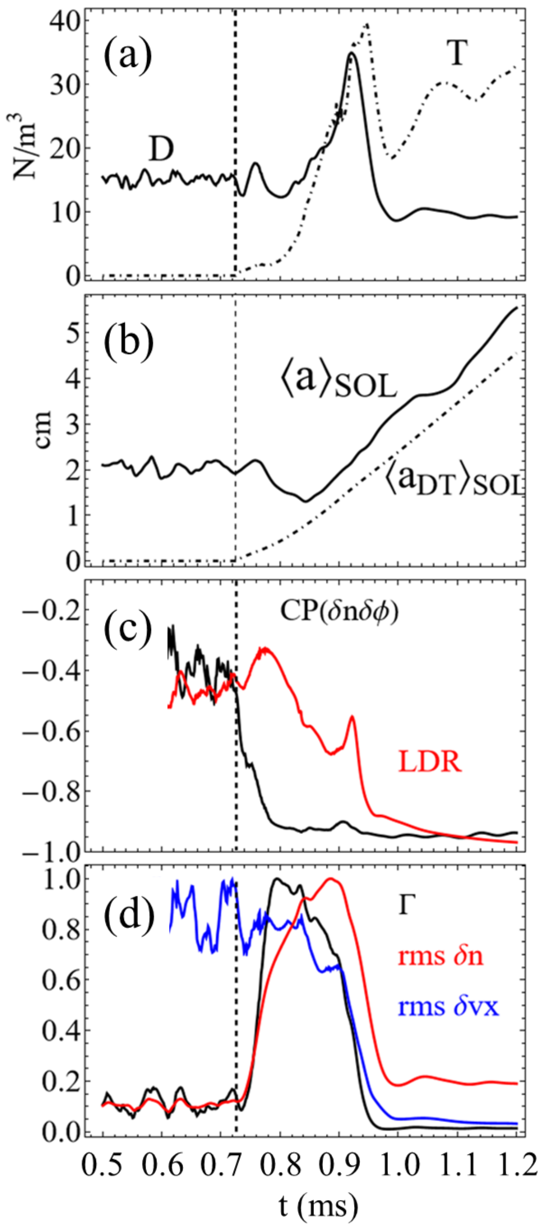

Fig. 10. Histories of (a) dipole (D) and tripole (T) polarizing forces [Eqs. (12)]; (b) the average width of density fluctuations in the SOL, $\langle a \rangle_{y,\Delta x>0}$, and the average threshold blob size for stagnation, $\langle a_{DT} \rangle_{y,\Delta x>0}$ [Eq. (13)]; (c) the cross-phase (CP) [Eq. (14)] for fluctuations from the simulation (black) and for the unstable mode of the linear dispersion relation (LDR) [Eq. (7a)]; and (d) the rms density (δn) and radial velocity (δv_x) fluctuation, and the radial particle flux from Fig. 4(b). All measurements are taken at $\Delta x = 1.7$ cm, except (b). The wave numbers were taken to be $k_x = 0$ and $k_y = 1.40$ cm^{-1} in the LDR.in (c). In (d) all quantities are rescaled to have maximum values of unity for comparison. [Associated dataset available at https://doi.org/10.5281/zenodo.7254770] (Ref. 39).

The curvature dipole (D) and CX tripole (T) vorticity sources from the simulation are compared in Fig. 10(a). We restrict the calculation to the fluctuating parts of the pressures and plot the root-mean-squares of the two sources with respect to y:

$$D = \beta\left\langle \left(\partial_y \delta P\right)^2 \right\rangle_y^{1/2}, \tag{12a}$$

$$T = \nu_{cx}\left\langle \left(\partial_y^2 \delta P_i\right)^2 \right\rangle_y^{1/2}. \tag{12b}$$

The CX drive overtakes the curvature drive at approximately t = 0.875 ms, where the D and T terms first cross, and dominates it after t = 0.925 ms. Blobs for which the tripole drive is stronger than the dipole drive (T > D) are expected to be radially non-propagating, viz., to be “stagnant.” The time required for T to overtake D in Fig. 10(a) is consistent with the time for the perpendicular flux ($\Gamma_\perp$) to be reduced to approximately zero in Fig. 4(b).

A threshold width for blob stagnation (a_{DT}) is found by associating the y-derivatives in Eqs. (12) with the reciprocal blob size, $\partial_y \rightarrow a^{-1}$, and equating D and T:

$$a_{DT} = \nu_{cx} / [\beta(1+T_e/T_i)] \rightarrow \frac{\nu_{CX} R}{2\Omega_i (1+T_e/T_i)}, \tag{13}$$

where the second form for a_{DT} is given in dimensional variables. This threshold is essentially the one found in Sec. III(b) for the LDR frequency to be dominantly real [Eq. (8d) with $k_y \rightarrow a^{-1}$, and $T_i > T_e$]. The result is a shift in the unstable spectrum satisfying $\omega_I > \omega_R$ to lower k_y. Thus, with growing ν_{cx}, smaller blobs experience stagnation before larger blobs, and the mean blob size in the SOL grows larger as a result. In the far-SOL, larger-scale blobs dominate the blob population because the smaller-scale blobs, moving more slowly, are drained away in the parallel direction before they can get out that far.

The mean bi-normal (y) blob size and a_{DT}, both averaged over the SOL, are plotted versus time in Fig. 10(b). The average blob size increases in parallel with a_{DT} and is of similar magnitude, but saturates at 6 cm, on the order of the fundamental bi-normal mode, radially sheared by the mean flow. The tripole mechanism described here, giving large blobs a higher velocity and later stagnation than small blobs, is different from the blob-size-dependent effects induced by neutrals that are discussed in Ref. [26]; in particular, the tripole mechanism depends on finite T_i.

The cross-phase (CP) is a measure of the correlation between the plasma density and electrostatic potential fluctuations that is often used to analyze turbulence,

$$CP = \left\langle \delta\phi\delta n\right\rangle_y \Big/ \left(\left\langle \delta\phi^2 \right\rangle_y^{1/2} \left\langle \delta n^2 \right\rangle_y^{1/2} \right). \tag{14}$$

The optimal cross-phase for radial blob propagation [e.g., $\delta n \sim \sin(k_y y)$ and $\delta\phi \sim \cos(k_y y)$, so $\delta v_x = -\partial_y \delta\phi \sim \delta n$] corresponds to CP = 0. This blob-propelling phase shift between δn and $\delta\phi$ is predicted by the LDR when the interchange drive is dominant: From the linearized density continuity equation and Eq. (8a), we find $\delta n(k_y) = ik_y \bar{n}' \delta\phi(k_y)/(\gamma_{mhd}^2 / \omega_s)$, giving CP = 0. On the contrary, if CP = ±1, [e.g., $\delta n \sim \sin(k_y y)$ and $\delta\phi \sim \sin(k_y y)$, so $\delta v_x \sim \cos(k_y y)$], the radial velocity, δv_x , is out of phase with δn, resulting in no net radial motion of the blob. This non-propagating phase relation between δn and $\delta\phi$ is predicted by the LDR in the large-ν_{cx} limit where the frequency ω is purely real. See Eq. (8b).

The cross-phase, Eq. (14), is plotted versus time at the reference location in Fig. 10(c). The figure suggests a transition from a turbulence more likely populated by radially propagating blobs to one in which blobs are less likely to be propagating. But the relatively sudden decrease in the cross-phase occurs before tripole polarization (T) has grown to compete with dipole polarization (D) in Fig. 10(a), and it occurs as the perpendicular flux is increasing in Fig. 10(d). [The perpendicular flux is reproduced from Fig. 4(b), where it is given in physical units, but all three quantities are rescaled to have maximum values of unity for comparison.] Furthermore, the amplitude of the radial velocity fluctuations, plotted in Fig. 10(d), remains approximately at its pre-neutrals value until T overtakes D, after which it decreases, causing the drop in the perpendicular flux that terminates the burst.

It is straightforward to show that the CP for fluctuations (δn, $\delta\phi$) satisfying the LDR, Eq. (7a), is

$$CP_{LDR} = \frac{-\bar{n}'k_y}{\left|\bar{n}'k_y\right|}[1+\omega_I^2 / (\omega_R - \omega_E)^2]^{-1/2}, \tag{15}$$

which is plotted (red) in Fig. 10(c) for the unstable branch of the LDR. Although Eq. (15) is for a single plane wave, and the LDR excludes much physics found in the full simulation, it is seen to be reasonably consistent with the result for the full simulation (black). Furthermore, it returns zero if the growth rate dominates the real part of the frequency (in the plasma frame), e.g., the purely growing interchange mode, and ±1 if the frequency is purely real, consistent with the above description of Eq. (14).

The initial fall of the cross-phase toward minus one, upon the onset of recycling, is caused by the rapid fall of the electron and ion temperatures due to IZ and CX cooling, respectively, seen in Fig.4(a). As a result of this cooling, the interchange growth rate γ_{mhd}, Fig. 5(a), and the imaginary part of the LDR-predicted frequency, Fig. 6(b), fall even before the CX damping rate has grown appreciably. The decrease in ω_I reduces the dipole charge polarization drive of the blobs, tending to move the amplitude of the cross-phase closer to unity, consistent with Eq. (15), suggesting non-propagation. Yet, the radial velocity fluctuation persists at its pre-burst amplitude until the DT transition.

The persistence of the radial velocity fluctuation, and the burst in the particle flux, are not necessarily inconsistent with the fall of the CP, Eq. (14), seen in Fig. 10(c), with the onset of the burst. The particle flux is by definition related to the cross-phase between the density and the radial *velocity* fluctuation, viz., $\Gamma_\perp = \langle \delta n \delta v_x \rangle_y \equiv \mathrm{CP}(\delta n, \delta v_x) \langle \delta n^2 \rangle_y^{1/2} \langle \delta v_x^2 \rangle_y^{1/2}$. Both the velocity fluctuation and the cross-phase, in this expression, continue through the burst at roughly their pre-burst (strictly positive) values, and the burst in $\Gamma_\perp$ is dominated by the burst in $\langle \delta n^2 \rangle_y^{1/2}$ seen in Fig. 10(d).

Snapshots of the electrostatic potential fluctuation ($\delta\phi$) at three different times are shown in Fig. 11. Before neutral turn-on (a), the turbulence consists of relatively small-scale, large-amplitude blobs. Soon after neutral turn-on, T_e and δT_e decrease due to ionization cooling. See Fig. 4(a). And, while the plasma is connected to the sheath ($\phi \sim \phi_B \cong 3T_e$), the amplitude of the potential fluctuation decreases as well, as seen by comparing Figs. 11(a) and 11(b). The factor of roughly ½ by which $|\delta\phi|$ is reduced differs from the factor of roughly 1/8 by which T_e has fallen, partly because the plasma is becoming disconnected from the sheath. (See Fig. 8.) Finally, in the wake of the burst, Fig. 11(c), the smaller blobs (larger k_y), immobilized by stagnation, have been removed from the SOL by parallel transport which persists in the absence of perpendicular transport. [See Fig. 4(b).] The remaining potential fluctuation is dominated by the fundamental mode ($k_y = 2\pi/L_y$), radially modulated by a sheared, bi-normal E×B flow.

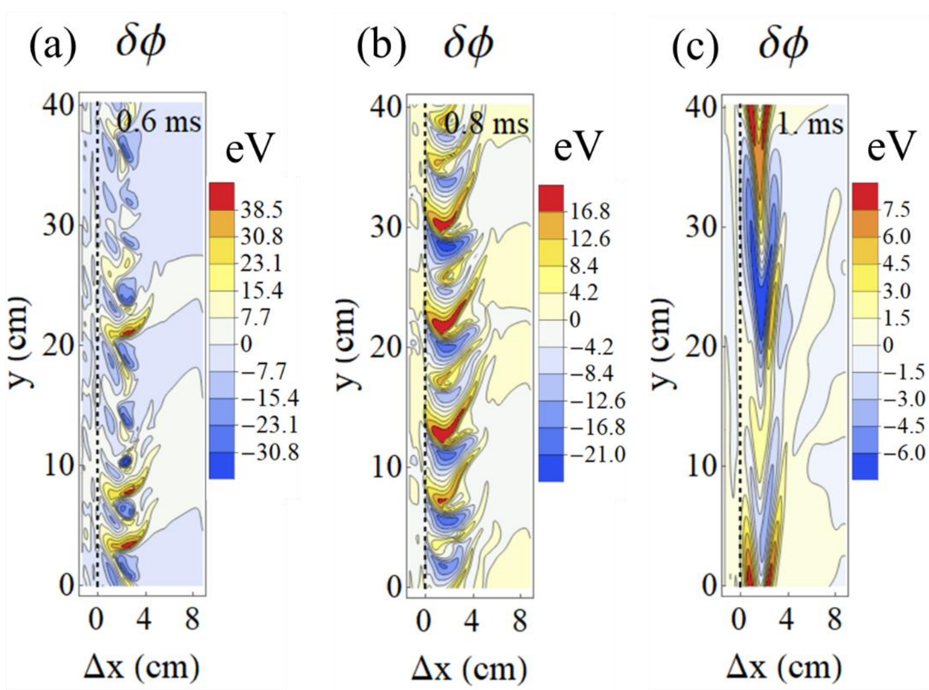

Fig. 11. Snapshots of the electrostatic potential fluctuation at (a) t = 0.6 ms, before the start of neutral recycling, (b) t = 0.8 ms, after the start of neutral recycling and with disconnection in-progress, and (c) t = 1.0 ms, after small-scale blobs, rendered radially non-propagating by CX

friction, have been removed from the SOL by parallel transport. [Associated dataset available at https://doi.org/10.5281/zenodo.7254770] (Ref. 39).

IV. Parallel heat and particle fluxes

a. Particle flux

The history of the electron parallel particle flux is shown in Fig. 4(a), in comparison with the perpendicular turbulent flux. It is seen that the parallel flux, $\Gamma_{\|e}$, increases to a maximum value approximately 4.4 times its pre-neutrals value and then relaxes to about twice its pre-neutrals value in the wake of the burst. The electron and ion fluxes are approximately equal after neutral turn-on because $\phi \cong \phi_B$, and, from Eqs. (A1) through (A7) in Ref. [7], we find $\Gamma_{\|e} = \Gamma_{\|i} = nc_s$. When the flux is at its maximum, the plasma density has increased by a factor of 8, while the sound speed has decreased roughly by a factor of 0.55. So, the increase in the parallel flux is dominated by the increase in the plasma density from the ionization source, despite the decrease in the sound speed due to ionization and CX cooling.

b. Heat flux

The electron and ion parallel heat fluxes are shown in Fig. 4(c), and expressions for them are given by Eqs. (A16) and (A17), respectively, in Ref. [7]. The power sent to the divertor is found by integrating the fluxes over the SOL ($\Delta x > 0$),

$$P_{div} = 2\pi R_m b_\theta \int_{\Delta x > 0} dx \left(Q_{\|e} + Q_{\|i} \right). \tag{16a}$$

The electron and ion contributions to P_{div} are plotted in Fig. 12(a).

The heat flux widths are taken to be the Loarte lengths,[38] given by

$$\lambda_{Le,i} = \int_{\Delta x > 0} Q_{\|e,i} dx / Q_{\|e,i}(\Delta x = 0), \tag{16b}$$

and are plotted for the electron and ion heat fluxes in Fig. 12(b). [In Eqs. (16), $Q_{\|e,i}$ represents the bi-normal (y) average of the heat flux.]

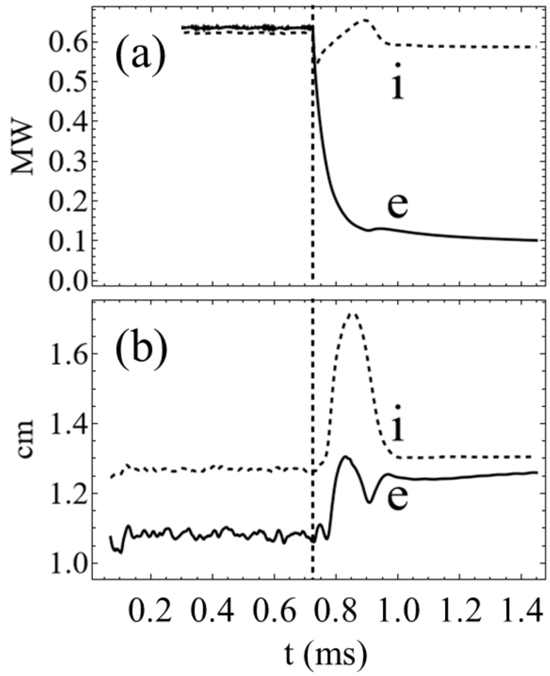

Fig. 12. (a) The power sent to the divertor, i.e., integral over the SOL of the parallel heat flux, in the electron (e) and ion (i) channels. (b) The electron and ion Loarte heat flux widths. [Associated dataset available at https://doi.org/10.5281/zenodo.7254770] (Ref. 39).

The electron heat flux is the sum of conductive ($q_{||e}$) and convective ($\sim \Gamma_{||e}$) components, viz.,

$$Q_{||e} \cong q_{||e} + \frac{5}{2} T_e \Gamma_{||e} . \qquad (17a)$$

(The additional term involving $j_{Padé}$ in Eq. (A16) of reference [7] proves to be ignorable in the simulation and is omitted here.) Since the ions are flowing into the sheath at the sound speed, which is on the order of the ion thermal velocity, the heat flux should be dominated by convection. A diffusive parallel heat conduction description is not appropriate in this limit, and the ion flux is purely convective,

$$Q_{||i} = \frac{5}{2} T_i \Gamma_{||i} . \qquad (17b)$$

Following neutral turn-on, the conductive flux, $q_{||e}$, decreases rapidly with the electron temperature. [Since $\phi \to \phi_B$, $q_{||e} \to q_{||CL} \sim T_e^{7/2}$, c.f., Eqs. (A12) through (A15) of Ref. [7]] This rapid loss of approximately half of the pre-neutrals flux dominates the drop in $Q_{||e}$ at the reference location seen in Fig. 4(c). With $q_{||e}$ ignored in Eq. (17a), the ratio of ion to electron powers is equal to that of the SOL-averaged convective fluxes, $Q_{||i} / Q_{||e} \cong \langle T_i \Gamma_{||i} \rangle / \langle T_e \Gamma_{||e} \rangle$. This ratio is 7/4 before neutral turn-on and rises steadily to 6 in the wake of the burst, consistent with the ratio of ion to electron powers in Fig. 12(a). We note that although the SOL-averaged ion and electron particle fluxes are equal, the heat flux ratio differs from the temperature ratio because $\langle T_i \Gamma_{\|i} \rangle \neq \langle T_i \rangle \langle \Gamma_{\|i} \rangle$, etc. We find that $\langle T_i \rangle / \langle T_e \rangle$ is 2.3 before neutral turn-on and rises steadily to 10 in the wake of the burst.

The electron and ion heat flux widths ($\lambda_{Le,i}$) increase with the onset of recycling, reaching maximum values equal to 1.2 and 1.3 times their pre-neutrals values, respectively, before relaxing to 1.15 and 1.02 of their pre-neutrals values in the wake of the burst. In other words, the post-burst heat flux widths are not significantly increased by the introduction of neutrals, particularly in the case of the ions, in comparison with the pre-burst widths. However, the blob influence on the profiles is apparent in the outward radial bulges seen in Fig. 3 at times before and during the burst. Similar features are seen in the profiles of the parallel heat fluxes plotted in Fig. 13. The post-burst equilibrium profiles lack these bulges and are approximately Gaussian shapes suggestive of a combination of radial diffusion and ionization of the given sources (S_n, $S_{Pe,i}$); the burst has removed the turbulent contribution to the widths that are dominated by the diffused sources at the end of the simulation. This is a new equilibrium compared to that reached in the pre-burst, turbulent phase of the simulation.

Comparing Figs. 4(c), 8 and 12(a) it is seen that the sharp drop in $Q_{\|e}$ and in electron parallel heat flux at the divertor is well correlated with electrical disconnection from the sheath, whereas the effect of disconnection on the ion flux is not so pronounced. It is tempting to speculate on the relationship of sheath connectivity to divertor detachment; however, definitive answers on that would require more sophisticated modeling of the parallel dynamics than our present reduced model can provide.

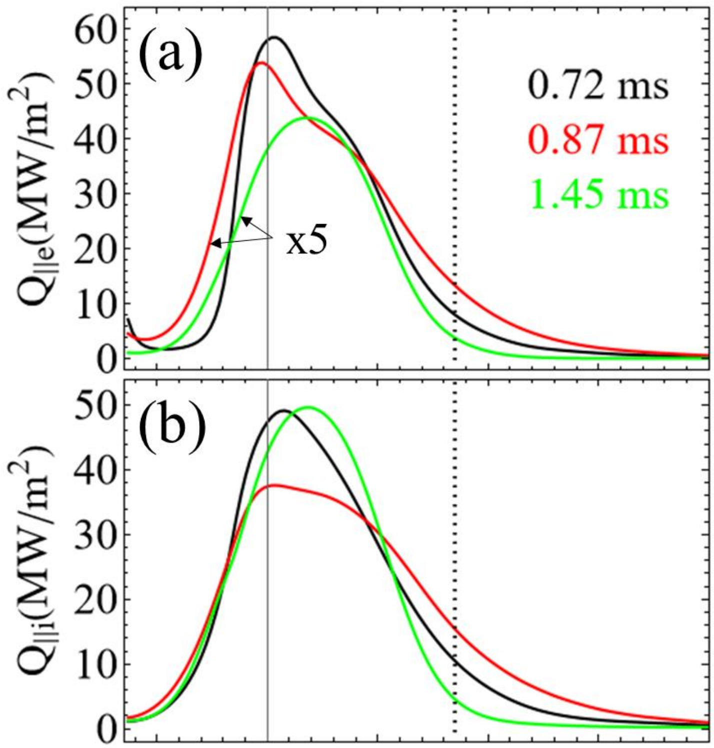

Fig. 13. Profiles of the parallel heat flux in the electron (a) and ion (b) channels at times before (black), during (red) and after (green) the burst. The burst (red) and post-burst (green) electron heat flux profiles in (a) have been multiplied by a factor of 5 to make them comparable to the pre-burst profile (black) in the plot. [Associated dataset available at https://doi.org/10.5281/zenodo.7254770] (Ref. 39).

V. Summary and Discussion

We presented results from a single nSOLT simulation in which an equilibrium turbulent plasma was exposed to a sudden influx of neutral atoms driven by plasma recycling at the divertor. The physical parameters and geometry of the simulation were chosen to model conditions at the divertor entrance on the MAST-U tokamak. The neutral population was evolved by a 1D kinetic equation and interacted with the fluid plasma through charge-exchange and ionization. Upon the introduction of neutrals, a transient burst of cross-field turbulent particle flux ($\Gamma_\perp$) occurred, followed by the emergence of a quiescent non-turbulent ($\Gamma_\perp \rightarrow 0$) plasma equilibrium in an atmosphere of growing neutral density in which the interchange instability was so moderated by CX damping, and the growth rate (γ_{mhd}) so reduced by ionization and CX cooling, that turbulence could not re-emerge. We analyzed the burst to determine the nature of its origin and extinction.

With regard to the onset of the burst, it has been shown in other work,[2,3] that the CX damping of the mean E×B flow (v_{Ey}) and its shearing rate ($\partial_x v_{Ey}$) can diminish shear-stabilization of the underlying instability and/or lower transport barriers that a shear layer may provide, potentially unleashing a burst similar to the one seen in the present simulation.

However, there is no evidence that the sheared mean flow is mitigating the interchange-driven turbulence in the pre-neutrals phase of the turbulence here. A local linear dispersion relation (LDR), Eq. (7a), was derived from the model equations of evolution and its predicted frequency compared favorably with that of the dominant modes extracted from the power spectra of fluctuations from the simulation. The pre-neutrals dominant mode was shown to be the sheath-moderated interchange mode, $\omega = \omega_E + i\gamma_{mhd}^2 / \omega_S$, and the saturation mechanism was found to be profile gradient modification.

For this simulation, there is also no evidence that the shearing rate falls prior to the onset of the burst. Instead, it was found that the initial increase in the plasma density fluctuation (δn) was at the ionization rate and, with little immediate change in the radial velocity fluctuation (δv_x), that increase dominated the initial rise in perpendicular transport ($\Gamma_\perp = \delta n \delta v_x$). Subsequently the ionization rate decreased with falling T_e, due to ionization cooling, and the growth of δn ceased.

We derived an expression for the shearing rate, Eq. (10), from the model evolution equations. Although it clearly demonstrates the ability of CX damping to reduce the shearing rate in principle, the damping is negligible in determining the equilibrium shearing rate, in comparison with sheath physics, for the parameters of the simulation. Indeed, we found that the shearing rate is fairly approximated by the second derivative of the equilibrium sheath potential, Eq. (11), at all times. See Fig. 7.

The fact that sheath or collisional physics dominates over charge exchange friction in the evolution of the equilibrium sheath potential is a consequence of the short connection length in the region of the divertor plasma considered here. In regions of the plasma where the connection length is longer, and hence α_{sh} in Eq. (10) is smaller, or on closed flux surfaces where $\alpha_{sh} = 0$, charge exchange flow damping is more likely to dominate the evolution of the turbulence, as noted in previous investigations. With decreasing T_e and increasing n_e the plasma grew more collisional. While the parallel current was sheath-limited before neutral recycling began, it was disconnected and conduction-limited soon thereafter. We used the ratio of sheath-to-collisional conductivities as a measure of disconnection and demonstrated the disconnection of blob filaments during the burst. See Figs. (8) and (9).

While blobs are usually observed to speed up upon disconnection,[9] their radial motion may be halted if, in the presence of a growing neutral population, the charge exchange force overtakes the curvature force in the vorticity equation. This change corresponds to a transition in the LDR from a purely growing mode, $\omega \sim i\gamma_{mhd}$, driven by the interchange force, to one with strictly real frequency found in the limit of growing charge-exchange damping,

$\omega = \omega_{*i} + i\gamma_{mhd}^2/\nu_{CX} \to \omega_{*i}$. According to the blob correspondence principle, $v_b \sim \omega_I / k_y$, that transition results in blob stagnation, $v_b \to 0$, where the condition for stagnation is $|\omega_{*i}|\nu_{CX} > \gamma_{mhd}^2$, or for $T_i > T_e$, $k_y \nu_{CX} > \beta$, in dimensionless units. See Sec. III(b) and III(e).

We compared the interchange force (denoted "D" for the dipole charge ~ $\partial_y P$ that it induces in a blob) and the CX friction force (denoted "T" ~ $\partial_y^2 P$ because it induces a non-propagating tripole charge distribution in a blob) acting on fluctuations. See Fig. 10(a). Turbulent transport ceases when T overtakes D, terminating the burst. A threshold width for blob stagnation (a_{DT}) was found by equating the D and T forces; blobs of (bi-normal) width 'a' are stagnant if a < a_{DT} and are drained away by parallel transport. The threshold a_{DT} is consistent with the threshold found from analysis of the LDR (with $k_y \to 1/a$) given above. It was shown that the measured average blob width in the SOL increases during the burst, and thereafter, at the same rate as a_{DT}. See Fig. 10(b).

The cross-phase, $\langle \delta\phi\delta n\rangle_y / \langle \delta\phi^2\rangle_y^{1/2} \langle \delta n^2\rangle_y^{1/2}$ drops to –1, suggesting stagnation, well before the DT transition, due to the initial fall of T_e and T_i caused by IZ and CX cooling, respectively, upon the onset of recycling. However, the r.m.s. radial velocity fluctuation, $\langle (\partial_y \delta\phi)^2 \rangle$, and the perpendicular flux, $-\langle \delta n \partial_y \delta\phi \rangle$, decrease abruptly only at the DT transition. See Fig. 10(d).

The introduction of neutrals significantly reduced the electron parallel heat flux to the divertor. This reduction was dominated by ionization cooling, particularly as the conductive heat flux $q_{||e}$ transitioned from sheath-limited (~T_e) to collision-limited (~$T_e^{7/2}$) when the parallel current was disconnected from the sheath. Consequently, the power to the divertor in the electron channel was reduced by a factor of 1/6. The effect of charge-exchange cooling on the ion channel was relatively insignificant. Similarly, the electron heat flux width increased by 15% with the introduction of neutrals while the ion width increased by 2%. See Fig. 12.

In conclusion, the present simulations have captured the synergies on turbulence of a number of individually well-known effects that will be present in a divertor plasma including recycling, ionization and associated cooling, charge exchange and associated friction, sheared flows and sheath connection (or not). The analysis has revealed an ionization-driven transport burst, electrical sheath disconnection, driven by ionization cooling and increased collisionality, blob stagnation from a combination of neutral friction and ion diamagnetism, and the mitigation of the parallel electron heat flux with little change in the SOL heat flux width. As experiments with the MAST-U divertor science station were not available at the time of this research, no attempt was made to simulate particular experiments; the present model simulation results are predictions that await experimental validation. It is hoped that these reduced model simulations in simplified geometry will stimulate the search for such effects in experiments and other turbulence codes.

Acknowledgements

This material is based on work supported by the US Department of Energy Office of Science, Office of Fusion Energy Sciences under award numbers DE-FG02-97ER54392 and DE-SC0019270.

Data Availability Statement

The data that support the findings of this study are openly available in Zenodo at https://doi.org/10.5281/zenodo.7254770, Ref. 39.

Appendix A Linear dispersion relation

We derive the local linear dispersion relation (LDR), Eq. (7a) of section IIIb, as follows.

A reduced vorticity evolution equation is obtained by ignoring the ion FLR and centrifugal terms on the second line of Eq. (3b), as well as the y-component of the friction force f_y. The curvature force (~**κ**) is in the negative radial (x) direction and competes with the radial component of the friction force, and we would like to emphasize that competition. So, we start from the reduced, linearized vorticity evolution equation:

$$\partial_t \delta\rho + v_E \partial_y \delta\rho = \frac{2}{R_m} \partial_y (\delta P_e + \delta P_i) - \partial_y \nu_{cx} n \left(\delta v_x + \delta v_{dix} \right) - \nabla_{\|} \delta j_{\|}. \tag{A1}$$

With the Fourier conventions $\partial_t \to -i\omega$ and $\nabla \to i\mathbf{k}$, we have $\delta\rho = k^2 \left(n\delta\phi + \delta P_i \right)$, $(-i\omega + ik_y v_E)\delta P_{e,i} = -\delta v_x P'_{e,i} = ik_y \delta\phi P'_{e,i}$ (from pressure continuity), and $\delta v_{dix} = -ik_y \delta P_i / n$. Here the zero-order fields (n, ϕ, $P_{e,i}$, $T_{e,i}$) are represented by their poloidal (y) averages, and the prime denotes the radial (x) derivative. Furthermore, we express invariance along the magnetic field lines by assigning to the operator $\nabla_{\|}$ in (A1) the value $(+)1/L_{\|}$, where $L_{\|}$ is the parallel connection length to the divertor target plate. The plus sign (+) is consistent with our convention that the charge density (vorticity) *decreases* with time where $\delta j_{\|}$ is *positive*. With these substitutions, (A1) becomes

$$-i\tilde{\omega} k^2 \left(n - \frac{k_y}{\tilde{\omega}} P'_i \right) \delta\phi = -i \frac{k_y^2}{\tilde{\omega}} \frac{2}{R_m} (P'_e + P'_i) \delta\phi - \nu_{cx} k_y^2 \left(n - \frac{k_y}{\tilde{\omega}} P'_i \right) \delta\phi - \delta j_{\|} / L_{\|}, \tag{A2}$$

where $\tilde{\omega} = \omega - k_y v_E$ is the frequency in the E×B drift frame, and ω is the frequency in the lab (simulation) frame.

The total parallel resistivity is the sum of the collisional (C) resistivity in the volume and the sheath (S) resistivity, or, in terms of conductivities (σ),

$$1/\sigma = 1/\sigma_S + 1/\sigma_C \,. \tag{A3}$$

With total and partial current density fluctuations given by

$$\delta j_{\parallel} = -\sigma \nabla_{\parallel} \delta\phi, \tag{A4}$$

$$\delta j_{\parallel S} = -\sigma_S \nabla_{\parallel} \delta\phi, \tag{A5.1}$$

$$\delta j_{\parallel C} = -\sigma_C \nabla_{\parallel} \delta\phi, \tag{A5.2}$$

it follows from (A3) that

$$\delta j_{\parallel} = \left(1/\delta j_S + 1/\delta j_C\right)^{-1}, \tag{A6}$$

which is the Padé expression used in the nSOLT model, written here for fluctuations.[7] (We ignore a flux-limiting partial current, proportional to the electron thermal speed, that appears as a third term in (A3) and (A6), because it is too large to be an effective limit in the simulation. See Eq. (A4) of reference [7].)

The parallel sheath conductivity (σ_S) is found by linearizing the expression for the sheath-limited current,

$$j_{\parallel S} = n_e c_s e\left(1 - e^{e(\phi_B - \phi)/T_e}\right), \tag{A7}$$

in fluctuations about the Bohm potential, $\delta\phi = \phi - \phi_B$, and the equilibrium temperature. In equilibrium, $\phi = \phi_B = 3T_e$, and we have

$$\delta j_{\parallel S} = \frac{n_e c_s e^2}{T_e}\left(\delta\phi - \frac{\phi}{T_e}\delta T_e\right) = -\sigma_S \nabla_{\parallel} \delta\phi . \tag{A8}$$

Using the continuity equation for T_e, and retaining only the convective time derivative, we obtain

$$\delta T_e = -\frac{c k_y T_e{}'}{B\tilde{\omega}} \delta\phi . \tag{A8.1}$$

Then letting $T_e' = e\phi'/3$, expressing δT_e in terms of $\omega_E = (c/B)k_y\phi'$, and substituting into Eq. (A8) we obtain

$$\delta j_{\parallel S} = \frac{e^2 n_e c_s}{T_e}\frac{\omega}{\tilde{\omega}}\delta\phi = -\sigma_S \nabla_{\parallel} \delta\phi . \tag{A8.2}$$

Here, we enforce the assumption of invariance along the field lines by replacing $\nabla_{\parallel}$ in (A8.2) with $-1/L_{\parallel}$. With this substitution it follows from (A8.2) that

$$\sigma_S = \frac{n_e c_s e^2 L_\parallel}{T_e} \frac{\omega}{\tilde{\omega}} . \tag{A9}$$

With the parallel collisional conductivity given by [40]

$$\sigma_C = \frac{n_e e^2}{0.51 m_e \nu_{ei}} , \tag{A10}$$

we have

$$\frac{\sigma_S}{\sigma_C} = 0.51(1 + T_i / T_e)^{1/2} \frac{\omega}{\tilde{\omega}} \Lambda , \tag{A11}$$

where Λ is the Coulomb collisionality parameter,

$$\Lambda \equiv \frac{\nu_{ei} L_\parallel}{\Omega_e \rho_{sr}} . \tag{A12}$$

Here ν_{ei} is the electron-ion collision frequency, and Ω_e is the electron cyclotron frequency. Using (A5.1), (A5.2), and (A11), (A6) may be written as

$$\delta j_\parallel = \frac{\sigma_S}{(1 + \hat{\Lambda})} (-\nabla_\parallel \delta\phi) , \tag{A13}$$

where

$$\hat{\Lambda} \equiv \frac{\sigma_S}{\sigma_C} = 0.51(1 + T_i / T_e)^{1/2} \frac{\omega}{\tilde{\omega}} \Lambda . \tag{A14}$$

Using (A13), with $\nabla_\parallel \to -1 / L_\parallel$, in (A2), and multiplying the result by $i\tilde{\omega} / nk^2$, yields the dispersion relation in the lab frame:

$$\left(\omega - \omega_E + i\,\hat{\nu}_{cx}\right)\left(\omega - \omega_E - \omega_{*i}\right) = -\gamma_{mhd}^2 - i(\omega - \omega_E)\omega_S \tag{A15}$$

where

$$\omega_E = k_y v_E , \tag{A17}$$

$$\hat{\nu}_{cx} = \nu_{cx} \frac{k_y^2}{k^2} , \tag{A18}$$

$$\omega_{*i} = k_y \frac{P_i'}{n} , \tag{A19}$$

$$\gamma_{mhd}^2 = -\frac{k_y^2}{k^2}\frac{2}{R_m}(P_e' + P_i')/n\,, \tag{A20}$$

and

$$\omega_S = \frac{c_s}{L_{\|}k^2\rho_s^2}\frac{\omega}{\tilde{\omega}}\left(1+\hat{\Lambda}\right)^{-1} \to \frac{\hat{\sigma}_S}{k^2 n L_{\|}^2}\left(1+\hat{\Lambda}\right)^{-1}, \tag{A21}$$

where the first form in Eq. (A21) expresses ω_S in terms of dimensional quantities (note $\rho_s^2 = \rho_{sr}^2 T_e / T_{er}$). In the expression for σ_S (A9), all quantities are in physical units. The dimensionless version, $\hat{\sigma}_S$ in (A21), is given by the same expression (A9) but without the factor e^2 and with all quantities given in dimensionless units,

$$\hat{\sigma}_S = \frac{n c_s L_{\|}}{T_e}\frac{\omega}{\tilde{\omega}}\,, \tag{A22}$$

where, again, all zero-order fields (n, ϕ, $P_{e,i}$, $T_{e,i}$) are represented by their poloidal (y) averages.

References

1 S. M. Kaye, R. Maingi, D. Battaglia, R. E. Bell, C. S. Chang, J. Hosea, H. Kugel, B. P. LeBlanc, H. Meyer, G. Y. Park, and J. R. Wilson, "L-H threshold studies in NSTX," Nucl. Fusion **51**, 113019 (2011).

2 D. P. Stotler, J. Lang, C. S. Chang, R. M. Churchill and S. Ku, "Neutral recycling effects on ITG turbulence," Nucl. Fusion **57**, 086028 (2017).

3 Y. Zhang and S. I. Krasheninnikov, "Effect of neutrals on the anomalous edge plasma transport," Plasma Phys. Control. Fusion **62**, 115018 (2020).

4 S. I. Krasheninnikov, A. S. Kukushkin, and A. A. Pshenov, "Divertor plasma detachment," Phys. Plasmas **23**, 055602 (2016).

5 D. S. Oliveira, T. Body, D. Galassi, C. Theiler, E. Laribi, P. Tamain, A. Stegmeir, M. Giacomin, W. Zholobenko, P. Ricci, H. Bufferand, J. A. Boedo, G. Ciraolo, C. Colandrea, D. Coster, H. de Oliveira, G. Fourestey, S. Gorno, F. Imbeaux, F. Jenko, V. Naulin, N. Offeddu, H. Reimerdes, E. Serre, C. K. Tsui, N. Varini, N. Vianello, M. Wiesenberger, C. Wüthrich and the TCV Team, "Validation of edge turbulence codes against the TCV-X21 diverted L-mode reference case," Nucl. Fusion **62,** 096001 (2022).

6 D. A. Russell, J. R. Myra, and D. P. Stotler, "A reduced model of neutral-plasma interactions in the edge and scrape-off-layer: verification comparisons with kinetic Monte Carlo simulations," Phys. Plasmas **26**, 022304 (2019).

7 D. A. Russell, J. R. Myra, F. Militello, and D. Moulton, "Reduced-model scrape-off layer turbulence (nSOLT) simulations comparing three fueling scenarios," Phys. Plasmas **28**, 092305 (2021).

8 S. I. Krasheninnikov, D. A. D'Ippolito, and J. R. Myra, J. Plasma Physics 74, 679 (2008).

9 D. A. D'Ippolito, J. R. Myra and S. J. Zweben, Phys. Plasmas **18**, 060501 (2011).

10 D .P. Stotler, J. Lang, C. S. Chang, R. M. Churchill, and S. Ku, "Neutral recycling effects on ITG turbulence," Nucl. Fusion **57**, 086028 (2017).

11 X. Q. Xu, R. H. Cohen, T. D. Rognlien, and J. R. Myra, "Low-to-high confinement transition simulations in divertor geometry," Phys. Plasmas **7**, 1951 (2000).

12 F. Riva, F. Militello, S. Elmore, J. T. Omotani, B. Dudson,N. R. Walkden, and the MAST team, "Three-dimensional plasma edge turbulence simulations of the Mega Ampere Spherical Tokamak and comparison with experimental measurements," Plasma Phys. Control. Fusion **61** 095013 (2019).

13 S. I. Braginskii, "Transport processes in a plasma," *Rev. Plasma Phys.* **1** 205 (1965).

14 B. LaBombard, "KN1D: A 1-D Space, 2-D Velocity, Kinetic Transport Algorithm for Atomic and Molecular Hydrogen in an Ionizing Plasma," Plasma Science and Fusion Center, MIT (2001). https://library.psfc.mit.edu/catalog/reports/2000/01rr/01rr003/01rr003_full.pdf

15 B. D. Dudson, H. R. Wilson, M. V. Umansky, X. Q. Xu, P. B. Snyder, "BOUT++: a framework for parallel plasma fluid simulations," Comput. Phys. Commun. **180** (9), 1467 (2009).

16 Z. H. Wang, X. Q. Xu, T. Y. Xia, and T. D. Rognlien, Nucl. Fusion **54**, 043019 (2014).

17 N. Bisai, Santanu Banerjee, and Deepak Sangwan, "Modification of plasma flows in edge and SOL regions by influence of neutral gas," Phys. Plasmas **25**, 102503 (2018).

18 J. Leddy, B. Dudson, and H. Willet, "Simulation of the interaction between plasma turbulence and neutrals in linear devices," Nucl. Mater. Energy **12**, 994 (2017).

19 A. S. Thrysøe, M. Løiten, J. Madsen, V. Naulin, A. H. Nielsen, and J. Juul Rasmussen, “Plasma particle sources due to interactions with neutrals in a turbulent scrape-off layer of a toroidally confined plasma,” Phys. Plasmas **25**, 032307 (2018).

20 C. Wersal and P. Ricci, “A first-principles self-consistent model of plasma turbulence and kinetic neutral dynamics in the tokamak scrape-off layer,” Nucl. Fusion **55**, 123014 (2015).

21 H. L. Berk, D. D. Ryutov, and Yu. A. Tsidulko, “Temperature-gradient instability induced by conducting end walls,” Physics of Fluids B: Plasma Physics **3**, 1346 (1991).

22 R. H. Cohen and D. D. Ryutov, “Beam-type instabilities of the sheath in a grazing magnetic field,” Phys. Plasmas **4**, 905 (1997).

23 S. I. Krasheninnikov and A. I. Smolyakov, “Current convective instability in detached divertor plasma,” Phys. Plasmas **23**, 092505 (2016).

24 D. A. Baver, J. R. Myra, F. Militello, and D. Moulton, “Comparison of private flux region instability in conventional and super-X divertor configurations,” Phys. Plasmas **28**, 112510 (2021).

25 N. Walkden, F. Riva, J. Harrison, F. Militello, T. Farley, J. Omotani, B. Lipschultz, “The physics of turbulence localized to the tokamak divertor volume,” Communications physics, 5:139 (2022), https://doi.org/10.1038/s42005-022-00906-2

26 D. Schwörer, N. R. Walkden, B. D. Dudson, F. Militello, H. Leggate, and M. M. Turner, “Dynamics of scrape-off layer filaments in detached conditions,” Nucl. Fusion **60**, 126047 (2020).

27 P. Paruta, P. Ricci, F. Riva, C. Wersal, C. Beadle, and B. Frei, “Simulation of plasma turbulence in the periphery of diverted tokamak by using the GBS code,” Phys. Plasmas **25**, 112301 (2018).

28 P. Paruta, C. Beadle, P. Ricci, and C. Theiler, "Blob velocity scaling in diverted tokamaks: A comparison between theory and simulation," Phys. Plasmas **26**, 032302 (2019).

29 J. M. Canik, R. Maingi, S. Kubota, Y. Ren, R. E. Bell, J. D. Callen, W. Guttenfelder, H. W. Kugel, B. P. LeBlanc, T. H. Osborne, and V. A. Soukhanovskii, Phys. Plasmas **18**, 056118 (2011).

30 D. P. Stotler, F. Scotti, R. E. Bell, A. Diallo, B. P. LeBlanc, M. Podestà, A. L. Roquemore, and P. W. Ross, "Midplane neutral density profiles in the National Spherical Torus Experiment," Phys. Plasmas **22**, 082506 (2015).

31 M.J. Seaton, "Radiative Recombination of Hydrogen Ions," Mon. Not. Roy. Astron. Soc. **119**, 81 (1959).

32 S. T. Zalesak, "Fully multidimensional Flux-Corrected Transport algorithms for fluids," J. Comput. Phys. **31**, 335–362 (1979); S. T. Zalesak, "The design of flux-corrected transport (FCT) algorithms for structured grids," D. Kuzmin et al. (eds.), Flux-Corrected Transport, Scientific Computation, DOI 10.1007/978-94-007-4038-9_2, © Springer Science+Business Media Dordrecht 2012, pg. 23.

33 W. H. Press, S. A. Teukolsky, W. T. Vetterling and B. P. Flannery, *Numerical Recipes in Fortran 77: The Art of Scientific Computing*, 2nd Edition, Cambridge University Press (1999), pg. 847.

34 J. R. Angus and M. V. Umansky, "Modeling of large amplitude plasma blobs in three-dimensions," Phys. Plasmas **21**, 012514 (2014).

35 H. L. Berk, R. H. Cohen, D. D. Ryutov, Yu. A. Tsidulko, and X. Q. Xu, Nucl. Fusion **33**, 263 (1993).

36 A. V. Nedospasov, "Turbulence near wall in tokamaks," Sov. J. Plasma Phys. **15**, 659 (1989).

37 K. H. Burrell, "Effects of $\boldsymbol{E}\times\boldsymbol{B}$ velocity shear and magnetic shear on turbulence and transport in magnetic confinement devices," Phys. Plasmas **4**, 1499–1518 (1997).

38 A. Loarte, S. Bosch, A. Chankin, S. Clement, A. Herrmann, D. Hill, K. Itami, J. Lingertat, B. Lipschultz, K. McCormick, R. Monk, G. D. Porter, M. Shimada, and M. Sugihara, "Multi-machine scaling of the divertor peak heat flux and width for L-mode and H-mode discharges," J. Nucl. Mater. **266–269**, 587–592 (1999).

39 Russell, David A., Myra, James R., & Militello, Fulvio. (2022). "A reduced-model (nSOLT) simulation of neutral recycling effects on plasma turbulence in the divertor region of MAST-U," Zenodo. https://doi.org/10.5281/zenodo.7254770

40 J. D. Huba, NRL Plasma Formulary, pg. 37, (2002), Naval Research Laboratory, Washington, D. C.